J. Fluid Mech. (2011), *vol.* 687, *pp.* 72–117.
doi:10.1017/jfm.2011.321

Transition to turbulence in toroidal pipes

Ivan Di Piazza‡ and Michele Ciofalo†

Dipartimento dell'Energia, Università degli Studi di Palermo, Viale delle Scienze, I-90128 Palermo, Italy

(Received 30 June 2010; revised 1 July 2011; accepted 22 July 2011;
first published online 18 October 2011)

Incompressible flow in toroidal pipes of circular cross-section was investigated by three-dimensional, time-dependent numerical simulations using a finite volume method. The computational domain included a whole torus and was discretized by up to $\sim 11.4 \times 10^6$ nodes. Two curvatures δ (radius of the cross-section/radius of the torus), namely 0.3 and 0.1, were examined; a streamwise forcing term was imposed, and its magnitude was made to vary so that the bulk Reynolds number ranged between ~3500 and ~14 700. The results were processed by different techniques in order to confirm the spatio-temporal structure of the flow. Consecutive transitions between different flow regimes were found, from stationary to periodic, quasi-periodic and chaotic flow. At low Reynolds number, stationary flow was predicted, exhibiting a symmetric couple of Dean vortex rings and a strong shift of the streamwise velocity maximum towards the outer wall. For $\delta = 0.3$, between $Re = 4556$ and $Re = 4605$ a first transition occurred from stationary to periodic flow, associated with a supercritical Hopf bifurcation and giving rise to a travelling wave which took the form of a varicose streamwise modulation of the Dean vortex ring intensity. A further transition, associated with a secondary Hopf bifurcation, occurred between $Re = 5042$ and $Re = 5270$ and led to a quasi-periodic flow characterized by two independent fundamental frequencies associated with distinct travelling waves, the first affecting mainly the Dean vortex rings and similar to that observed in purely periodic flow, the second localized mainly in the secondary flow boundary layers and manifesting itself as an array of oblique vortices produced at the edge of the Dean vortex regions. Both the periodic and the quasi-periodic regimes were characterized by an instantaneous anti-symmetry of the oscillatory components with respect to the equatorial midplane of the torus. For $\delta = 0.1$, between $Re = 5139$ and $Re = 5208$ a direct ('hard') transition from steady to quasi-periodic flow occurred. Hysteresis was also observed: starting from a quasi-periodic solution and letting the Reynolds number decrease, both quasi-periodic and periodic stable solutions were obtained at Reynolds numbers below the critical value. A further decrease in Re led to steady-state solutions. This behaviour suggests the existence of a subcritical Hopf bifurcation followed by a secondary Hopf bifurcation. The resulting periodic and quasi-periodic flows were similar to those observed for the higher curvature, but the travelling modes were now instantaneously symmetric with respect to the equatorial midplane of the torus. Also, the further transition from quasi-periodic to chaotic flow occurred with different modalities for the two curvatures. For $\delta = 0.3$, a centrifugal instability of the main flow in the outer region occurred abruptly between $Re = 7850$ and $Re = 8160$, while a further increase of Re up to 13 180 did not cause any relevant change in the distribution and intensity of the fluctuations. For $\delta = 0.1$ the transition to chaotic flow was gradual in the range $Re = 6280$ to 8160

† Email address for correspondence: ciofalo@din.unipa.it
‡ Current address: ENEA UTIS-TCI, C.R. Brasimone, 40032 Camugnano(Bo), Italy.

and affected mainly the inner region; only a further increase of *Re* to 14 700 caused fluctuations to appear also in the outer region.

Key words: pipe flow boundary layer, transition to turbulence, turbulence simulation

1. Introduction

1.1. *Relevance and realizability of the flow in a closed torus*

In this paper computational fluid dynamics is used to study the flow regimes that establish themselves when an incompressible fluid flows in toroidal pipes for different values of the curvature and of the Reynolds number.

The interest of the toroidal pipe flow configuration stems from the fact that it is the common asymptotic limit of two distinct classes of important flow problems.

(*a*) Flow in curved pipes and bends. While entry effects may be important in this problem, several studies, including all the earliest work starting with Boussinesq (1868) and Dean (1927), have been conducted under the assumption of fully developed flow, which reduces this geometry to that of a toroidal pipe. A necessary condition for the assumption of fully developed flow to hold is that the curvature is small, so that the flow development length can be neglected in comparison to the length of the bend.

(*b*) Flow in helical pipes. This latter geometry is encountered in engineering applications such as heat exchangers and steam generators (Vashisth, Kumar & Nigam 2008). Theoretical and experimental studies on helical coils (Germano 1982; Kao 1987; Xie 1990; Chen & Jan 1992; Yamamoto *et al.* 1995; Jinsuo & Benzhao 1999) have shown that coil torsion, which differentiates a helical pipe from a toroidal one, has only a higher-order effect on flow features, so that a moderate torsion does not significantly affect global quantities.

Thus, any curved pipe can be studied as a toroidal pipe for sufficiently small and constant curvature, and any helically coiled pipe can be studied as a toroidal pipe for sufficiently small torsion. Of course, studying the (closed) toroidal configuration relieves one from the need to choose specific inlet–outlet boundary conditions but forces the solution to be 2π-periodic, which will affect some of the predicted flow features, notably involving streamwise patterns. Therefore, the results presented in this paper strictly apply only to a closed torus, and may not be representative of those that would be observed in open systems.

A problem with toroidal pipe flow is its realizability: unlike open configurations such as finite-length bends and coils, which allow a fluid to be mechanically pumped through the system, a closed torus requires the flow to be maintained by different causes. This explains why experimental studies on closed tori are rare in the literature. However, there are means by which a fully developed flow can be maintained in a closed torus.

A first possibility is magnetohydrodynamic pumping. In a toroidal pipe having a major radius c and a minor radius a filled with a fluid of electrical conductivity σ, an electrical potential difference ΔV applied between the inner and outer sides of the torus in a vertical magnetic induction field B will give rise to a streamwise force per unit volume $p_s = \sigma B \Delta V/(2a)$. For example, for $c = 0.5$ m, $a = 0.05$ m, $B = 10^{-3}$ T, $\Delta V = 40$ V and $\sigma = 5$ S m^{-1} (sea water) one has $p_s = 2$ Pa m^{-1}, which is sufficient to keep water flowing at an average speed of $\sim$0.1 m s^{-1} ($Re \approx 10^4$).

A second possibility is provided by inertial forces; maintaining a torus of major radius c at an angular acceleration $\dot{\omega}$ is equivalent (in the non-inertial reference frame of the rotating torus) to applying a streamwise force per unit volume $\sim\rho\dot{\omega}c$. For the same configuration of the previous example, a Reynolds number of 10^4 can be obtained by an angular acceleration of just 4×10^{-3} rad s^{-2}. Of course, such conditions can be maintained only for a limited time, which, however, may be sufficient for fully developed flow to be attained.

Finally, if the requirement of steady-state flow is relaxed, a decelerating flow in a toroidal pipe can be studied by starting from initial conditions of rigid-body rotation and then stopping (more or less rapidly) the motion of the pipe; this technique was used, for example, by Del Pino *et al.* (2008).

In the following, the literature on flow in curved pipes will be reviewed, putting emphasis on instability and transition in order to place the present computational results in the appropriate context.

1.2. *Secondary flow in curved pipes*

Flow in curved pipes is characterized by the existence, even at low Reynolds numbers, of a secondary circulation in the cross-section, caused by the imbalance between inertial and centrifugal forces. Literature reviews for flow in curved pipes have been presented by Berger, Talbot & Yao (1983) and by Naphon & Wongwises (2006). The earliest qualitative observations on the complexity involved can be found in Boussinesq (1868); the author shows clear insight into the correct leading mechanisms of the secondary flow, and predicts the presence of two symmetric secondary vortices in a curved closed duct. Thomson (1876) interpreted the erosion effects on the outer side of river bends as an effect of the secondary circulation. Williams, Hubbell & Fenkell (1902) observed that the location of the maximum streamwise velocity is shifted towards the outer wall of a curved pipe, and Grindley & Gibson (1908) observed the effect of curvature on the fluid flow during experiments on the viscosity of air. Later, Eustice (1911) showed the existence of a secondary flow by injecting ink into water. Einstein (1926), in a well-known brief paper, discussed the physical mechanisms driving secondary flows in river bends and the formation of meanders.

A more quantitative approach to the problem was proposed by Dean (1927), who wrote the Navier–Stokes equations in the local toroidal frame of reference (r, θ, s) in which r and θ are polar coordinates in the generic cross-section and s is the abscissa along the axis of the pipe (streamwise direction). Under the hypothesis of small curvature and laminar stationary flow, he derived a solution for the stream function of the secondary motion and for the main streamwise velocity, both expanded in power series whose first term corresponded to Hagen–Poiseuille flow. Dean's solution exhibits a shift of the streamwise velocity maximum towards the outer wall and two symmetric secondary cells with characteristic velocity scale

$$\hat{u}_{sec} \approx \hat{u}_{av}\sqrt{\delta}, \tag{1.1}$$

in which $\hat{u}_{av}$ is the average streamwise velocity, δ is the non-dimensional curvature a/c, a is the radius of the section and c is the radius of curvature. Here and in the following, dimensional quantities will be indicated by a caret ($\hat{}$), while no caret will be used for dimensionless quantities.

The bulk Reynolds number Re is defined as

$$Re = \hat{u}_{av}2a/\nu. \tag{1.2}$$

The Dean number is defined as

$$De = Re\sqrt{\delta} \tag{1.3}$$

and takes account of inertial, centrifugal and viscous effects. For small values of the curvature, De becomes the single governing parameter. The Dean number plays a role similar to that of the Taylor number $Ta = \Omega^2 R_1 (R_2 - R_1)^3/\nu^2$ used in the context of Taylor–Couette flow between concentric cylinders of radii R_1 and R_2 with relative angular velocity Ω; identifying R_1 with c, $(R_2 - R_1)$ with $2a$, and Ω with $\hat{u}_{av}/c$, one has $De = \sqrt{Ta/2}$.

From Dean's solution, an analytical expression can be derived for the ratio of flow rates in slightly curved pipes and straight pipes under the same forcing. This ratio can be expressed as a series of powers of the Dean number (Van Dyke 1978), and is less than 1 in the series' radius of convergence.

McConalogue & Srivastava (1968) obtained two-dimensional stationary semi-analytical solutions by expanding the flow variables in Taylor series of the azimuthal angle and then integrating numerically the resulting ordinary differential equations in the radial coordinate. They showed that the secondary flow field is not self-similar, but its shape changes with the Dean number: in low-Dean-number flows its streamlines are almost elliptic in shape and are roughly symmetric with respect to the vertical midline of the cross-section, while, as De increases, the maximum streamwise velocity shifts towards the outer side of the pipe, and the centres of the secondary circulation towards the inner side.

Other analytical asymptotic studies based on power series expansions have been presented in recent decades. Larrain & Bonilla (1970) studied the asymptotic case of fully developed creeping flow in curved pipes at low curvatures (coiled capillaries). They showed that, when the Reynolds number is negligibly small, the mass flow rate in slightly curved pipes under a given forcing term actually increases with respect to a straight pipe because, contrary to intuition, the streamwise velocity maximum shifts towards the inner side of the pipe, thus shortening the mean fluid path.

1.3. *Transition to turbulence in curved pipes*

Most of the first attempts to determine the conditions for transition to turbulence in curved (and, in particular, helical) pipes focused on the behaviour of global quantities such as the friction coefficient. The earlier departure from the linear pressure drop/flow rate behaviour observed in curved pipes with respect to straight pipes was interpreted in these studies as an indication of an earlier transition to turbulence. However, after the work of Dean (1927) and the experiments of Taylor (1929), it became clear that the departure from linearity in the pressure drop/flow rate relationship is simply an indication that the flow in curved pipes is not self-similar, as observed in the previously cited study by McConalogue & Srivastava (1968), rather than an indication of departure from laminar flow conditions. Most of the increased resistance in curved pipes is due to the secondary circulation, and a stationary laminar flow is actually maintained in curved pipes up to Re well above the critical value for straight pipes. Narasimha & Sreenivasan (1979) showed that, in a helically coiled pipe preceded and followed by straight segments, under appropriate conditions turbulent flow may be maintained in these latter while the flow remains laminar in the coils.

White (1929) observed that, at least for sufficiently low curvatures, all the experimental data on the friction factor ratio (curved/straight) taken below a critical Reynolds number (different for each curvature) collapse on a single 'universal' curve if they are reported as functions of the Dean number; when this critical Re is

exceeded, the data depart from the 'universal' curve. This observation leads to a possible operative definition of the transitional Reynolds number for each curvature.

In more recent studies too, transition to turbulence in curved and helical pipes has been investigated mainly on the basis of pressure drop data.

Experimental results for a wide range of curvatures and Reynolds numbers were presented by Ito (1959), who derived the following correlations for the Darcy–Weisbach friction factor f (four times the Fanning coefficient) in the laminar and turbulent ranges:

$$f = \frac{64}{Re}\frac{21.5De}{(1.56+\log_{10}De)^{5.73}} \quad \text{(laminar flow)}, \tag{1.4}$$

$$f = 0.304Re^{-0.25} + 0.029\sqrt{\delta} \quad \text{(turbulent flow)} \tag{1.5}$$

valid for $5\times10^{-4} \leqslant \delta \leqslant 0.2$.

Despite being dated, (1.4) and (1.5) have recently been confirmed to an impressive degree by the extensive experimental work of Cioncolini & Santini (2006) in a wide range of curvatures ($0.027 \leqslant \delta \leqslant 0.143$) and Reynolds numbers ($Re \approx 10^3$–$7\times10^4$). For relatively high values of the curvature ($0.0416 \leqslant \delta \leqslant 0.143$), the friction coefficient decreased monotonically with Re and transition to turbulence was indicated by a change in slope of the f–Re curve. Therefore, for sufficiently high curvatures, an indicative value of the critical Reynolds number for transition to turbulence can be provided by the intersection of fully laminar and fully turbulent asymptotic laws. An approximate correlation which expresses this criterion for the critical Reynolds number is

$$Re_{cr} = 2100(1+15\delta^{0.57}). \tag{1.6}$$

For lower curvatures ($\delta < 0.0416$), Cioncolini & Santini (2006) observed that in the proximity of transition the f–Re curves exhibited a local minimum followed by an inflection point and by a local maximum; different transition criteria may be specified on the basis of different features of the f curves, but may not coincide with the actual onset of turbulence.

Further, the alternative transition correlations proposed by Ito (1959), Srinivasan, Nadapurkar & Holland (1970) and other authors are based on different interpretations of the $f(Re)$ behaviour for different δ, but do not really capture the specific dynamics of the transition process. All the proposed criteria, however, agree that the effect of curvature is to increase Re_{cr} with respect to straight pipes. For example, (1.6) predicts $Re_{cr} = 10\,580$ for $\delta = 0.1$; the case $\delta = 0.3$ is outside its range of validity.

Few studies have investigated transition in curved pipes by direct measurements of local flow quantities. Sreenivasan & Strykowski (1983) obtained experimental results in helically coiled pipes using Tygon^{TM} tubes wrapped around a cylinder, with a curvature ratio $\delta = 0.058$ and a negligible torsion. Two hot wires were positioned within a cross-section of the tube, one near the inner side and one near the outer side. Measurements were taken after five helix turns where the flow was fully developed, and the Reynolds number range investigated varied from 4200 to 6730. For $Re = 4200$ the hot wires registered flat signals corresponding to a laminar stationary flow. For $Re = 5000$, a periodically oscillating behaviour was observed in the inner region and a small-amplitude, high-frequency intermittent oscillation in the outer region. For $Re = 5870$, a not perfectly periodic behaviour was observed in the inner region, and a substantial intermittent turbulent oscillation in the outer region. For $Re = 6730$, the behaviour was fully turbulent both in the inner and in the outer region. The outer

side appeared to be the critical region for transition to a chaotic behaviour, since both intermittency and high frequencies first appeared there. The authors suggested that the instability was due to the vorticity and the angular velocity of the main flow being opposite in this region.

A similar conclusion can be derived by applying to the main (streamwise) flow the stability criterion initially proposed by Rayleigh (1920) and discussed, for example, by Chandrasekar (1970) in the context of Taylor–Couette flow between concentric cylinders. For a general flow with curved streamlines, the criterion can be formulated by introducing the discriminant

$$\phi(r) = \frac{1}{r^3}\frac{\partial}{\partial r}(ru_\varphi)^2 \tag{1.7}$$

(in which r is the radial direction and u_φ is the azimuthal velocity component), and stating that this must be positive for stability. Rayleigh based this criterion on the argument that, in regions where $\phi(r) > 0$, the radial displacement of a fluid element yields an imbalance between pressure and centrifugal forces which pushes it back towards its original position, whereas in regions with $\phi(r) < 0$ the imbalance pushes it further away.

Webster & Humphrey (1993) investigated flow in helical coils by LDV techniques for $Re \approx 3800$–$10\,500$ and $\delta \approx 5.5 \times 10^{-2}$. For Reynolds numbers between 5060 and 6330 ($De = 1190$–1480) the authors observed what they described as a periodic flow, characterized by a dimensionless frequency $f \approx 0.14$ (normalized by the reference frequency $\hat{u}_{av}/a$). They attributed the origin of the periodic flow to an instability of the outward-directed midplane jet. Transition to turbulence proper was observed only for $Re \geqslant 6330$. In later work (Webster & Humphrey 1997), the same authors performed flow visualization by dye streaks for the same curvature and Reynolds number range. On the basis of these new results, they identified the cause of flow periodicity in a travelling-wave instability of Dean vortices of the varicose type, i.e. one in which the axis of each vortex ring remains approximately a circumference, while the vortex intensity varies periodically streamwise (as opposed to a sinuous instability which would involve a periodic lateral oscillation of the vortex ring axes). For $Re = 5060$, they estimated the wavelength to be $(2\pi c)/20$ and the wave phase speed (celerity) to be $\sim 0.825\hat{u}_{av}$; these values changed little with the Reynolds number. The authors re-interpreted the origin of the travelling wave as due to a centrifugal instability of the secondary flow, occurring in the cross-stream wall layers and in the periphery of the Dean vortices, as suggested by the application of the Rayleigh criterion. It is worth noting that the experimental results of Sreenivasan & Strykowski (1983) for similar values of the curvature ($\delta = 5.8 \times 10^{-2}$) and of the Reynolds number ($Re \approx 5000$) are also compatible with a travelling-wave solution located mainly in the inner (Dean vortex) region, although the authors did not explicitly suggest this interpretation. Previous reports of travelling-wave phenomena deserve special attention since the present paper is largely devoted to the analysis of such structures.

1.4. *Computational studies*

Following the early studies mentioned in § 1.2, Van Dyke (1978) developed the extended Stokes series (ESS) method on the basis of Dean's solution. His results indicated that the friction factor ratio between curved and straight pipes should behave as $De^{1/4}$, while boundary layer techniques (Mori & Nakayama 1965) and numerical techniques (Collins & Dennis 1975) suggested a dependence upon $De^{1/2}$ for high Dean numbers in the laminar range. The discrepancy was addressed by Jayanti &

Hewitt (1991) and was explained by the slow convergence of the ESS expansion, which requires a very large number of terms to achieve accurate results. Siggers & Waters (2008) extended the Dean solution to the case of finite curvature and also studied conditions of oscillatory forcing.

A number of two-dimensional studies on transition and stability have been presented for curved ducts of circular (Dennis & Ng 1982) and square (Daskopoulos & Lenhoff 1989; Wang & Yang 2004) cross-section. These works used perturbation methods to study the amplification of disturbances in laminar stationary solutions under the assumption that there is no variation of any quantity along the duct axis. They show that four-vortex modes can develop as a second family of solutions at sufficiently high Dean numbers; this four-vortex flow is stable to symmetric disturbances but unstable to asymmetric ones (Yanase, Yamamoto & Yoshida 1994). In this latter work it is shown that, for the circular cross-section, the four-cell solution can be obtained only in an open region of the Re–δ plane and does not exist for $Re < 252$. For example, the critical Reynolds number for the appearance of a second-family, four-vortex solution is $\sim$380 for $\delta = 0.1$ and $\sim$240 for $\delta = 0.3$. Zabielski & Mestel (1998) suggested that there are no stable, steady four-vortex solutions in helical pipes.

These studies have a purely theoretical interest because the perturbation modes found are not the actual three-dimensional modes which develop in a three-dimensional configuration, e.g. the travelling-wave instability modes reported by Webster & Humphrey (1997) and those discussed later in the present study. As a terminology issue, it is worth noting that, in most works on square cross-section channels (Daskopoulos & Lenhoff 1989; Wang & Yang 2004), it is common to use the term 'Ekman vortices' for the first vortices which develop from the imbalance of centrifugal and inertial terms, whose equivalents in circular pipes are the original 'Dean vortices' found by Dean (1927), and earlier by Boussinesq (1868). The same works use 'Dean vortices' for the secondary vortices located in the outer region which develop at higher Dean numbers in four-cell solutions.

Three-dimensional numerical simulations of incompressible turbulent flow in helical and curved pipes were presented by Friedrich and co-workers (Hüttl & Friedrich 2001; Friedrich *et al.* 2001; Hüttl *et al.* 2004). They solved numerically the Navier–Stokes equations, written in the local orthogonal helical coordinate system proposed by Germano (1982), and compared toroidal and helical pipe results for $Re \approx 5600$ ($Re_\tau \approx 230$) and $\delta = 0.1$. Although the authors performed a statistical processing of the computational results (e.g. by computing Reynolds stress distributions in the cross-section), the case they studied was not actually turbulent, but rather a time-dependent laminar flow, as indicated by the experimental results obtained by Webster & Humphrey (1997) and Sreenivasan & Strykowski (1983) under similar conditions and by the results of the present study (see below). It must also be observed that in the simulations by Hüttl & Friedrich (2001) and Friedrich *et al.* (2001) only a small portion of pipe, 7.5 diameters long, was modelled, using periodic boundary conditions at the ends; such simulations would be inadequate to predict travelling waves.

Webster & Humphrey (1997) also complemented their experimental investigation by numerical simulations, performed by discretizing the Navier–Stokes equations written in the local toroidal reference frame, i.e. neglecting coil torsion. The length of the computational domain was chosen equal to the experimentally measured wavelength, thus forcing the travelling wave to possess *a priori* prescribed features. Under conditions in which experiments provided evidence for a travelling-wave instability, the numerical results showed oscillating velocities with maximum r.m.s. values in the

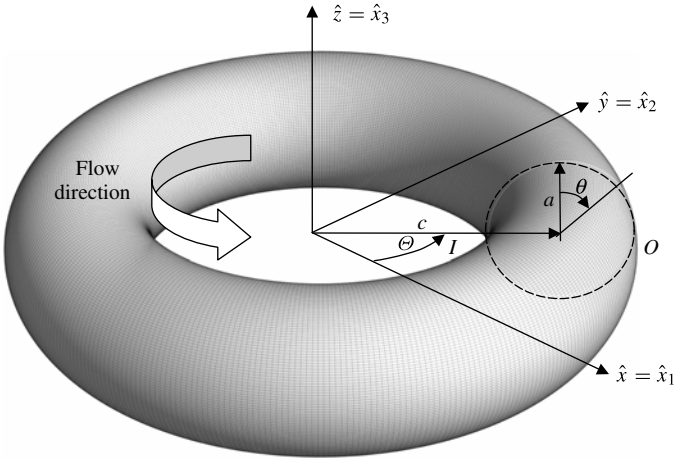

FIGURE 1. Schematic representation of a toroidal pipe with its main geometrical parameters: a, tube radius; c, coil radius. The inner (I) and outer (O) sides of the curved duct are also indicated; θ is the angular co-ordinate in the cross-section, measured clockwise with $\theta(I) = -\pi/2$, $\theta(O) = \pi/2$, while Θ is the angular displacement of the cross-section from the x-axis.

proximity of the Dean vortices. Quantitative comparison with experiments was not possible due to the purely qualitative (flow-visualization) nature of these latter.

Travelling waves in a curved square duct were found both experimentally and numerically by Mees, Nandakumar & Masliyah (1996). The travelling-wave mode developed from the stationary four-cell flow typical of curved square ducts, and was characterized by the oscillation of the outer vortices.

2. Models and methods

2.1. *Computational domain, governing equations, boundary and initial conditions*

The possible presence of travelling waves, indicated by previous studies as discussed in the Introduction, motivated our decision to choose as computational domain a full torus, where boundary conditions are not necessary in the streamwise direction since the domain is circularly closed, and travelling-wave instabilities can properly develop with physically consistent wavelengths.

Figure 1 shows a schematic representation of the torus; the major radius will be indicated with c, the minor radius with a. The inner side will be indicated with I and the outer side with O; here and in all the subsequent figures showing cross-sections of the pipe, the O side will be on the right and the I side on the left, and the view will be along the flow direction, i.e. looking from upstream. The cross-section azimuthal angle will be measured in the clockwise direction, with $\theta(I) = -\pi/2$, $\theta(O) = \pi/2$.

The continuity and Navier–Stokes equations for a constant-property fluid were solved in the Cartesian orthogonal reference frame $\hat{x}_j = (\hat{x}, \hat{y}, \hat{z})$ of figure 1. In dimensional form:

$$\frac{\partial \hat{u}_j}{\partial \hat{x}_j} = 0, \tag{2.1}$$

$$\frac{\partial \hat{u}_i}{\partial \hat{t}} + \frac{\partial \hat{u}_i \hat{u}_j}{\partial \hat{x}_j} = -\frac{1}{\rho}\frac{\partial \hat{p}}{\partial \hat{x}_i} + \frac{\partial}{\partial \hat{x}_j}\nu\frac{\partial \hat{u}_i}{\partial \hat{x}_j} + \frac{p_{s,i}}{\rho}. \tag{2.2}$$

A constant source term p_s (force per unit volume) directed along the axis of the pipe was adopted as the driving force balancing frictional losses, so that $p_{s,1} = -p_s \sin\Theta$, $p_{s,2} = p_s \cos\Theta$, $p_{s,3} = 0$, in which Θ is the azimuth around the torus axis z: see figure 1. This is equivalent to imposing the equilibrium mean shear stress $\hat{\tau}_0 = (a/2)p_s$ and the corresponding friction velocity $\hat{u}_\tau = \sqrt{\hat{\tau}_0/\rho}$. A friction Reynolds number $Re_\tau = \hat{u}_\tau a/\nu$ can be defined on the basis of this latter.

Although the simulations were conducted in a Cartesian orthogonal reference frame, for post-processing and discussion purposes a cylindrical reference frame $(\hat{r}_p, \Theta, \hat{z})$ was used for the whole torus, $\hat{r}_p$ being the normal distance from the torus axis z; the direction Θ of the main flow is also indicated by s (for 'streamwise') in the figures. A local two-dimensional polar reference frame $(\hat{r}, \theta)$ was used in the plane of the generic cross-section; the secondary flow in this plane may be alternatively represented by its components u_r, u_θ along $(\hat{r}, \theta)$ or by its components u_{rp}, u_z along $(\hat{r}_p, \hat{z})$.

No-slip conditions were imposed at the wall. Zero-velocity initial conditions were set for most of the numerical simulations; a few cases were restarted from a solution obtained for a higher Reynolds number, as discussed in § 5. Instabilities, if any, were triggered by small numerical fluctuations due to truncation and round-off errors.

2.2. *Scales*

Although the friction velocity $\hat{u}_\tau = \sqrt{(a/2)p_s/\rho}$ is the *a priori* known quantity, the average velocity $\hat{u}_{av}$ was chosen as the velocity scale. The corresponding frequency scale is

$$\hat{f}_0 = \frac{\hat{u}_{av}}{a} = \frac{Re}{2}\frac{\nu}{a^2} \tag{2.3}$$

proportional, by the factor $Re/2$, to the molecular momentum diffusion frequency ν/a^2. The time scale follows as $\hat{t}_0 = 1/\hat{f}_0$. The scale for angular velocity is naturally $\hat{\omega}_0 = 2\pi\hat{f}_0$; the wall shear stress was scaled by $\rho\hat{u}_{av}^2$.

All coordinates were scaled by the cross-section radius a; thus, the non-dimensional local radial coordinate, measured from the centre of the cross-section, is $r = \hat{r}/a$, while the non-dimensional distance of the generic point from the torus axis z is $r_p = \hat{r}_p/a$.

2.3. *Numerical method and computational mesh*

The computational method was based on a finite volume coupled algebraic multigrid solver, and adopted the central interpolation scheme for the advection terms and a second-order backward Euler time-stepping algorithm. The code simultaneously solves all the transport equations in a coupled fashion; the linearized system of equations is preconditioned in order to reduce all the eigenvalues to the same order of magnitude. The multigrid approach reduces the low frequency error, converting it to a high frequency error at the finest grid level; this results in a great acceleration of convergence. The computational domain was partitioned into equal-sized blocks which were assigned to different processes, generally running in parallel on 16 cores.

The mesh is multi-block-structured, and is characterized by the parameters N_{RAD} and N_θ as shown in figure 2. In the present work the values used are $N_{RAD} = 46$, $N_\theta = 24$ and grid refinement is used at the wall, with a maximum/minimum cell size ratio of $\sim$5 in the radial direction. With these choices, the cross-section is resolved by 11 136 cells. In the streamwise direction the domain is discretized by $N_{AX} = 1024$ cells for $\delta = 0.1$ and $N_{AX} = 300$ cells for $\delta = 0.3$; this leads to an overall number of cells of 11.4×10^6 for $\delta = 0.1$ and 3.34×10^6 for $\delta = 0.3$. The surface mesh for $\delta = 0.3$ is actually shown in figure 1.

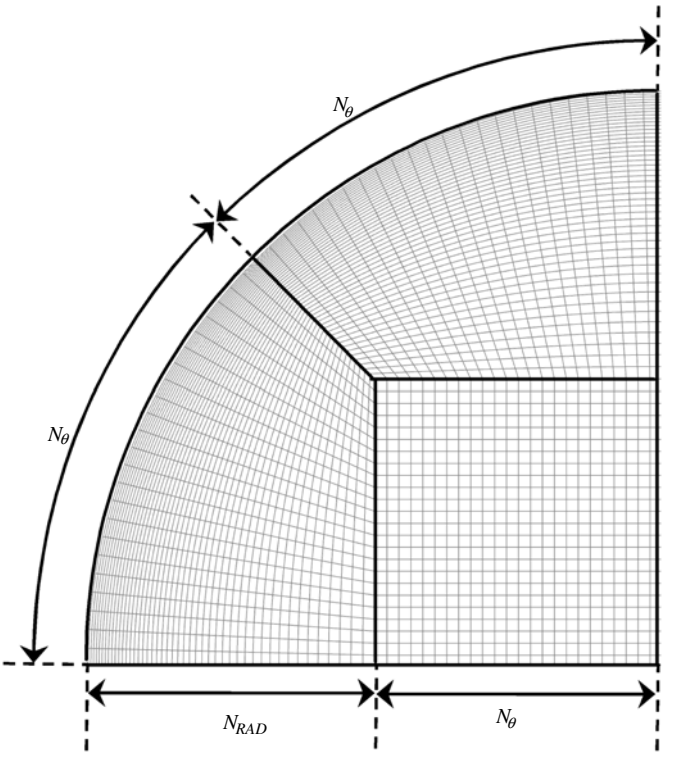

FIGURE 2. One quarter of the cross-section of the multi-block-structured computational mesh. The total number of cells in the whole cross-section is $N_{SEC} = 4N_\theta\ (N_\theta + 2N_{RAD})$.

Among the test cases simulated in this paper, those that put the highest demand on spatial resolution are the turbulent flow cases since a direct numerical simulation requires that all relevant scales, down to the Kolmogorov dissipative scale, are resolved by the computational grid. The Kolmogorov scale $\Lambda_K = (\nu^3/\varepsilon)^{1/4}$ can be estimated by identifying the turbulence energy dissipation ε with the total energy dissipation; for the present configuration, this assumption leads to

$$\Lambda_K = a/(\sqrt{Re_\tau} Re^{1/4}). \tag{2.4}$$

In flows with recirculation, this assumption is highly conservative since a considerable fraction of the total dissipation is associated with the secondary flow and not with turbulence. At $Re \approx 8000$, for both curvatures the present mesh provides a resolution of $\sim 6\Lambda_K$ in the streamwise direction and 3–$6\Lambda_K$ in the azimuthal direction. In the radial direction, the resolution is $\sim 1.3\Lambda_K$ on average, and ranges from $\sim 0.6\Lambda_K$ to $\sim 3\Lambda_K$, taking account of near-wall grid refinement. The first near-wall grid point is at $y^+ \approx 0.8$ and 4–5 grid points lie within the viscous sublayer ($y^+ \leqslant 11$). These values are adequate for a direct numerical simulation of turbulence and, of course, are more than adequate in the non-turbulent, lower-Reynolds-number cases; it should be stressed that in the present work emphasis is placed on time-dependent laminar or early chaotic flow rather than on fully turbulent flow.

The time step was set equal to $0.8(\nu/u_\tau^2)$ for all cases; this time discretization is sufficient to capture both the turbulent fluctuations (Choi & Moin 1994) and the

dynamic features of time-dependent laminar flows. For the present streamwise grid, this choice leads to a Courant number less than 1.

2.4. *Proper orthogonal decomposition*

Proper orthogonal decomposition (POD) was used, among other techniques, to process simulation results in the generic cross-section. This technique was introduced in fluid dynamics by Lumley (1967); a complete description is given by Berkooz, Holmes & Lumley (1993). It is based on a two-point correlation and is able to capture the highest possible variance of a given quantity for a given number of orthogonal eigenfunctions.

For a space- and time-dependent quantity Φ with time mean $\langle\Phi\rangle$, represented in discrete form by $\Phi_{i,k}$ (in which the index $i = 1, \ldots, N$ denotes spatial points and the index $k = 1, \ldots, M$ denotes time instants), the time covariance matrix $R_{ij} = (1/M)\sum_{k=1}^{M}(\Phi_{i,k} - \langle\Phi\rangle_i)(\Phi_{j,k} - \langle\Phi\rangle_j)$ is computed and the N eigenvalues α_l and eigenvectors Ψ_l of the associated operator are evaluated; Φ is then decomposed as

$$\Phi = \langle\Phi\rangle + \sum_{l=1}^{N} a_l(t)\Psi_l, \tag{2.5}$$

in which the generic term $a_l(t)\Psi_l$ is the product of the lth time-dependent coefficient by the lth spatial eigenvector. If Φ is defined in a two-dimensional domain (cross-section of the duct), Ψ_l is the discrete representation of the two-dimensional eigenfunction $\Psi_l(r, \theta)$; note that the dependence upon the streamwise coordinate s does not need to be explicitly considered since the present problem is homogeneous along s. The time-dependent coefficients $a_l(t)$ are computed by projecting the original data set into the new eigenfunctions basis. This decomposition does not postulate a particular shape for $\Psi_l(r, \theta)$, but finds the 'natural' spatial eigenfunctions of Φ. The fraction of variance contained in the lth eigenfunction is $\beta_l = \alpha_l / \sum \alpha_l$.

In the present work, POD was applied to two-dimensional distributions over the generic cross-section of the pipe, having area A; the spatial eigenfunctions $\Psi_l(r, \theta)$ were normalized so that

$$\frac{1}{A}\int_A |\Psi_l(r, \theta)|^2 \, \mathrm{d}A = 1, \tag{2.6}$$

while the amplitude of the associated orthogonal mode was expressed by the time-dependent coefficient $a_l(t)$, which retained the physical dimensions (or the dimensionless nature) of the primitive variable Φ.

3. Range of parameters investigated and flow regime transitions

In the present study, a systematic investigation was carried out for each curvature by letting the friction Reynolds number Re_τ vary from 232 to 519 ($\delta = 0.3$) or from 164 to 476 ($\delta = 0.1$). The corresponding bulk Reynolds number varied between 4515 and 13 180 for $\delta = 0.3$ and between 3490 and 14 700 for $\delta = 0.1$. For both curvatures, steady-state flow was predicted for $Re \leqslant Re_c$ and time-dependent flow for $Re > Re_c$, Re_c being a critical Reynolds number which was estimated to be ~4575 for $\delta = 0.3$ and ~5175 for $\delta = 0.1$. However, the transition scenario was different for the two curvatures as discussed below.

For the higher curvature $\delta = 0.3$, a full sequence of flow regimes from stationary (S) to periodic (P), quasi-periodic (QP) and chaotic (C) flow was observed, similar to that reported for Taylor–Couette flow between concentric cylinders (Fenstermacher, Swinney & Gollub 1979) and consistent with the classic Ruelle–Takens transition

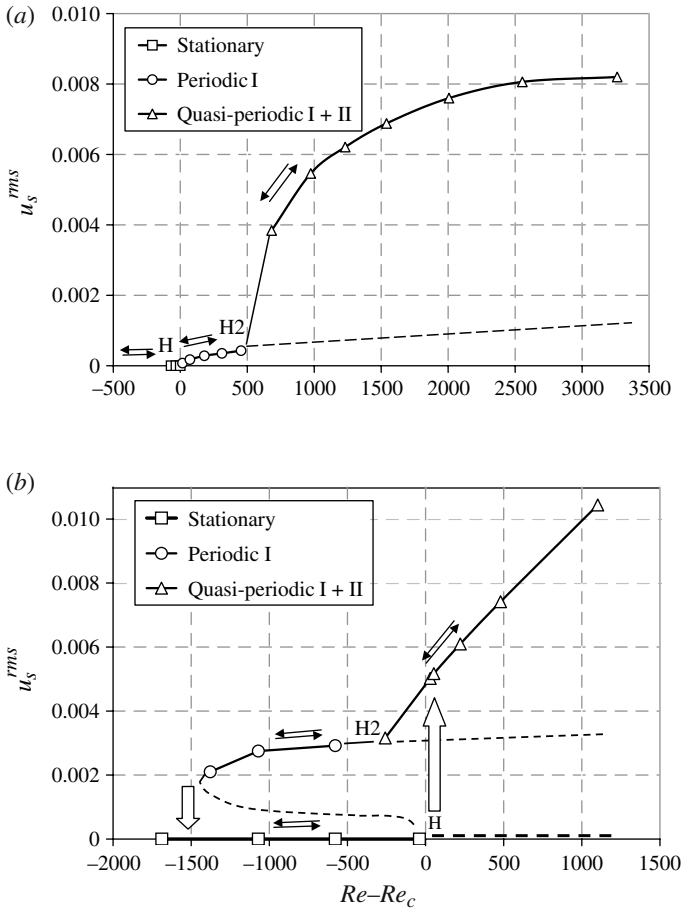

FIGURE 3. Bifurcation diagrams for $\delta = 0.3$ (*a*) and $\delta = 0.1$ (*b*). The abscissa is the difference between the Reynolds number Re and the Reynolds number Re_c of the Hopf bifurcation; the ordinate is the root mean square value of the oscillatory component of the streamwise velocity in a generic cross-section for $r = 0.8$, $\theta = -\pi/4$. H = Hopf bifurcation; H2 = secondary Hopf bifurcation; solid lines, stable branches; dashed lines, unstable branches.

route. This is illustrated in figure 3(*a*) by reporting the root mean square value u_s^{rms} of the oscillatory component of the streamwise velocity in a point of a generic cross-section located at $r = 0.8$, $\theta = -\pi/4$ as a function of the difference between the Reynolds number Re and the critical Reynolds number Re_c. The results indicate the existence of a supercritical Hopf bifurcation from stationary to periodic flow at $Re = Re_c$ (point H in the figure), followed by a secondary Hopf bifurcation from periodic to quasi-periodic flow at $Re \approx Re_c + 500$ ($Re \approx 5075$, point H2 in the figure). Symbols denote computational predictions; different symbols are used for S, P and QP solutions. Both the H and the H2 transitions were of the 'soft' type, i.e. a generic flow quantity like u_s^{rms} varied continuously as Re crossed the relevant bifurcation value. As discussed in detail in §§ 5.1 and 5.2, the transition from S to P flow was accompanied by a breaking of the instantaneous symmetry with respect to the torus midplane; the ensuing anti-symmetry was preserved also in the QP flow regime. Transition to

turbulence (not illustrated in figure 3*a* for scale reasons) occurred only at $Re \approx 8000$ ($\sim Re_c + 3500$).

For the lower curvature $\delta = 0.1$, a more complex sequence of flow regimes was observed. This is illustrated in figure 3(*b*), which reports the same quantity u_s^{rms} as in figure 3(*a*). In simulations starting either from zero velocity or from the immediately lowest-*Re* solution, an abrupt ('hard') transition from S to QP flow occurred when the Reynolds number exceeded $Re_c \approx 5175$. The QP regime was maintained up to a Reynolds number of $\sim$8000 as for $\delta = 0.3$. However, simulations conducted by starting from a QP case and reducing the Reynolds number *below* Re_c led to a QP solution for $Re = 4920$ ($Re - Re_c \approx -255$) and to P solutions for $Re = 4600$, 4108 and 3800 ($Re - Re_c \approx -575$, -1067 and -1375, respectively). Only a further reduction to $Re = 3490$ ($Re - Re_c \approx -1685$) led to steady-state flow. Thus, the results exhibited hysteresis: some solutions could be obtained only by approaching them backward from higher Reynolds numbers, and in a range of *Re* multiple solutions (S-P or even S-QP) were obtained for the same *Re* depending on the path followed. Interestingly, unlike case $\delta = 0.3$, all the P and QP solutions exhibited instantaneous symmetry with respect to the torus midplane. The limited number of test cases studied does not allow a full reconstruction of the relevant bifurcation diagram; however, that sketched in figure 3(*b*) is compatible with the existing results. It includes a subcritical Hopf bifurcation (H) at $Re = Re_c$ ($\sim$5175), an unstable periodic branch, a turning point between $Re \approx 3500$ and $Re \approx 4000$, a stable periodic branch and a secondary Hopf bifurcation (H2) at $Re \approx 4900$. To the best of the authors' knowledge, a comparable transition scenario has not been reported previously in the literature for other flows. Transition to turbulence is not illustrated in figure 3(*b*) for scale reasons.

Table 1 summarizes the eight selected test cases presented in detail in this paper. They cover the two values of the curvature $\delta = 0.3$ and $\delta = 0.1$, denoted by D3 and D1, and all four different regimes S, P, QP and C. Both Reynolds numbers *Re* and Re_τ are provided in table 1 along with the Dean number *De*. The friction factor can be computed simply by $f = 32(Re_\tau/Re)^2$, and its values predicted by Ito's resistance correlations (1.4)–(1.5) are also reported for comparison purposes; however, it should be observed that neither of (1.4) or (1.5) is strictly applicable to the cases with $\delta = 0.3$.

4. Stationary flow

Stationary flow was obtained for $Re = 4515$ and 4556 ($\delta = 0.3$) and for $Re = 3490$, 4108, 4600 and 5139 ($\delta = 0.1$). The two test cases D3-S ($\delta = 0.3$, $Re = 4556$) and D1-S ($\delta = 0.1$, $Re = 5139$) were chosen as representative. The corresponding values of Re_τ, *De* and other global quantities are reported in table 1. The higher values of the friction coefficient *f* obtained for D3-S with respect to D1-S are justified by the higher Dean number, and thus by the more intense secondary circulation associated with higher curvatures. Of course, since stationary solutions are strictly two-dimensional, a fully three-dimensional simulation would not have been necessary, but this can be stated only with hindsight.

Selected results for these two cases are reported in figure 4 in order to illustrate the main features of the flow, largely retained also in the unsteady cases, and to establish a basis of comparison for the subsequent time-dependent solutions presented in §§ 5 and 6. Figures 4(*a*) and 4(*c*) report contours of the streamwise velocity u_s in the upper half of the cross-section, and contours of the quantity $-Q$ in the lower half. *Q* is the

https://doi.org/10.1017/jfm.2011.321 Published online by Cambridge University Press

Case	D1-S	D1-P*	D1-QP	D1-C	D3-S	D3-P	D3-QP	D3-C
δ	0.1	0.1	0.1	0.1	0.3	0.3	0.3	0.3
Re_τ	217	184	232	305	234	247	290	361
Re	5139	4108	5658	8160	4556	4899	6128	8160
De	1625	1299	1789	2561	2495	2732	3356	4475
Regime	S	P	QP	C	S	P	QP	C
$f(\times 10^2)$	5.718	6.400	5.391	4.484	8.449	8.119	7.190	6.256
$f(\times 10^2)$ laminar, (1.4)	5.627	6.331	5.352	4.445	7.825	7.546	6.756	5.879
$f(\times 10^2)$ turbulent, (1.5)	n.a.	n.a.	n.a.	4.117	n.a.	n.a.	n.a.	4.786

TABLE 1. Synoptic table of the main test cases simulated. Each case is identified in the text by the shorthand in the first row. Flow regimes are indicated by S (stationary), P (periodic), QP (quasi-periodic), C (chaotic). *Condition attained only by letting Re decrease from case D1-QP.

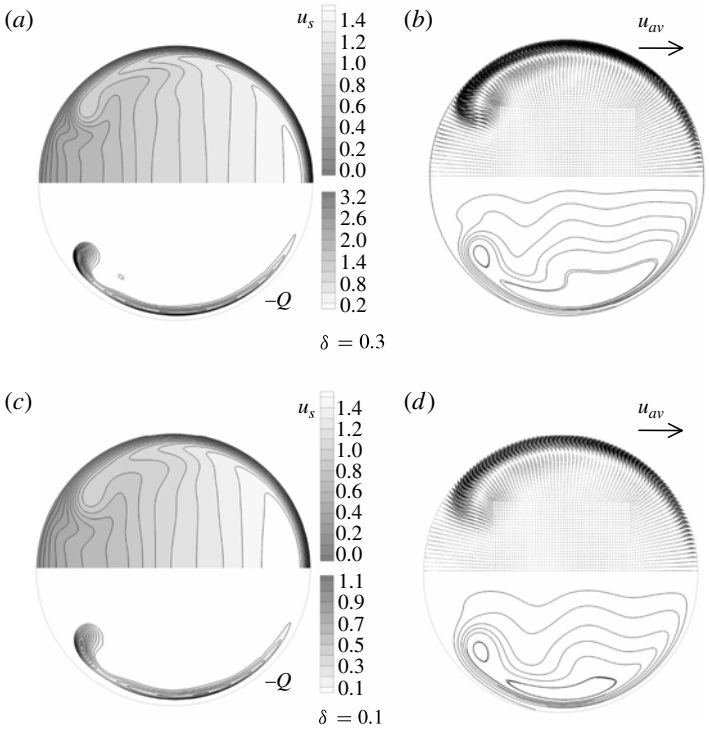

FIGURE 4. Dimensionless solutions for the stationary cases D3-S (a, b) and D1-S (c, d). (a,c) Streamwise velocity in the upper half and contours of the quantity $-Q$ (see text) in the lower half of the section. (b,d) Secondary flow vector plot (reference vector drawn besides) in the upper half and streamlines in the lower half of the section.

Okubo–Weiss parameter, defined as

$$Q = S_{ij}S_{ij} - \Omega_{ij}\Omega_{ij}, \tag{4.1}$$

where S_{ij} and Ω_{ij} are the projections of the strain rate and vorticity tensors, respectively, on the cross-section plane; the negative regions of Q define vorticity-dominated regions. Here, the usefulness of Q is related to the fact that, unlike vorticity, this quantity vanishes at the walls, making the identification of recirculation regions clear (Hunt, Wray & Moin 1988). Figures 4(b) and 4(d) report vector plots of the secondary motion in their top half, with the reference vector corresponding to $\hat{u}_{av}$ drawn, and corresponding streamlines in the bottom half. The solution is always symmetric with respect to the equatorial midplane of the torus.

Figures 4(a) and 4(c) show that the streamwise velocity maximum is shifted towards the outer (O) wall and that a roughly linear stratification of the streamwise velocity along the I–O direction exists in the core region. The shape and extent of the inner-wall vortices is typical of high-Dean-number flow and is consistent with numerical results obtained by other authors, e.g. Yanase, Goto & Yamamoto (1989) and Zabielski & Mestel (1998). In each of the twin vortices the streamlines are winding and strongly asymmetric with respect to the vertical midline of the section and exhibit two separate maxima, i.e. two closed-circulation regions; by contrast, in low-Dean-number flows the streamlines are almost elliptic in shape and are roughly symmetric with respect to the

vertical midline of the cross-section (Collins & Dennis 1975). Only minor differences are observed between the two curvatures.

Following a referee's suggestion, we tested the stability of the steady-state flow obtained for $\delta = 0.1$ and $Re = 4600 = Re_c - 578$ by superimposing a streamwise and azimuthally uniform axial velocity perturbation $u_p \cos[3\pi r/(2a)]$ on the stationary solution and restarting the simulation. For $u_p = 2\,\%$ of the mean axial velocity, following a transient of a few times a/u_τ the flow reverted to the stationary solution, thus confirming that this is stable at least to some finite-amplitude disturbances (of course, we know that the steady-state flow at this Re is unstable to travelling-wave disturbances of the appropriate structure and amplitude, as confirmed by the existence of a periodic solution sharing the same Reynolds number as shown by figure 3*b*).

5. Unsteady laminar flow

5.1. *Case D3-P* ($\delta = 0.3, Re = 4899$)

For $\delta = 0.3$ periodic flow was obtained for Reynolds numbers of 4605, 4660, 4768, 4899 and 5042. In particular, detailed results will be illustrated for case D3-P ($\delta = 0.3, Re = 4899$).

A general overview of the flow unsteadiness can be obtained by considering consecutive maps of the quantity $-Q$ on a generic cross-section (figure 5). Maps are taken at equal dimensionless time intervals of 0.84 starting from an arbitrary instant; during the time interval which separates the last from the first frame the fluid covers, on average, roughly 1/5th of the toroidal length. Periodic unsteadiness can be observed, mainly concentrated in the Dean vortex regions, whereas flow in the secondary boundary layers is almost stationary. The flow field is not symmetric with respect to the equatorial midplane.

Figure 6(*a*) reports short time samples of the streamwise velocity fluctuations $u_s - \langle u_s \rangle$ at two arbitrary points of the cross-section, one located in the upper secondary flow boundary layer and one in the upper Dean vortex region, over a dimensionless time interval of 30 starting from an arbitrary instant. The periodicity is clearly visible at both locations; oscillations are small ($\sim$0.6 %) in the Dean vortex region and even smaller ($\sim$0.03 %) in the secondary flow boundary layer region. Frequency spectra of the same two quantities, taken over a dimensionless time interval $\Delta t \approx 140$, are reported in figure 6(*b*). The signals relative to both monitoring locations exhibit a sharp peak at a dimensionless frequency of $\sim$0.238 (f^1); harmonics at $f = 2f^1$ and $3f^1$ are present in the Dean vortex region but negligible in the secondary flow boundary layer.

POD was directly applied to the results in order to confirm the spatial distribution of the oscillatory component of the flow. Figure 7(*a*) shows the first two spatial eigenfunctions Ψ_1^{I}, Ψ_2^{I} associated with the dimensionless streamwise velocity u_s; the corresponding time-dependent coefficients a_1^{I}, a_2^{I} are reported in figure 7(*b*). These first two eigenfunctions capture $\sim$97 % of the overall variance associated with the flow oscillations; as figure 7(*a*) shows, they are concentrated almost exclusively in the Dean vortex regions. The oscillation consists of a varicose wave travelling around the torus and involving mainly the three-dimensional Dean vortex rings; each spatial eigenfunction Ψ (and therefore the whole oscillatory component of the flow) is anti-symmetric with respect to the equatorial midplane. Thus, the varicose patterns associated with the two Dean vortex rings are arranged at any instant in a staggered fashion. The amplitude of the time-dependent coefficients in figure 7(*b*), expressing the intensity of the streamwise velocity fluctuations, is less than 1 %.

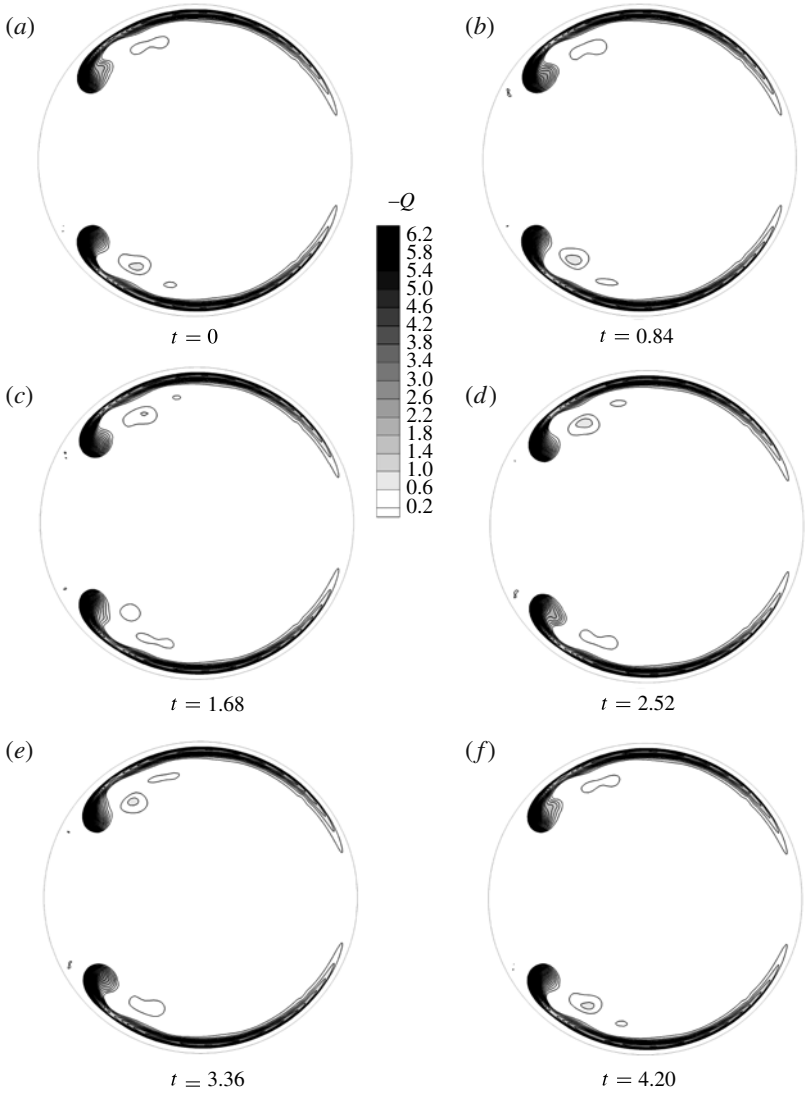

FIGURE 5. Maps of the quantity $-Q$ at dimensionless time intervals of 0.84 starting from an arbitrary instant on a generic cross-section for test case D3-P ($Re = 4899$, $\delta = 0.3$).

The spatial structure of the flow oscillations is more clearly visible in figure 8, which reports the instantaneous distribution of the vertical velocity component u_z on the equatorial midplane. This distribution exhibits $k^{\mathrm{I}} = 8$ cells and rotates rigidly along the torus with a dimensionless rotational celerity $F^{\mathrm{I}} = f^{\mathrm{I}}/k^{\mathrm{I}} \approx 0.0298$ (number of rotations in the reference time $a/\hat{u}_{av} = 1/\hat{f}_0$). The dimensionless linear celerity of the travelling wave, evaluated at the mean radius c, is $2\pi F^{\mathrm{I}}/\delta \approx 0.623$. Therefore, the wave celerity is less than the mean fluid velocity so that the wave lags behind the fluid over most of the toroidal volume.

All the periodic cases simulated for $\delta = 0.3$ (ranging from $Re = 4605$ to $Re = 5042$) exhibited the same wavelength number $k^{\mathrm{I}} = 8$. Also, the dimensionless modal frequency remained about constant ($\sim$0.238) in this range.

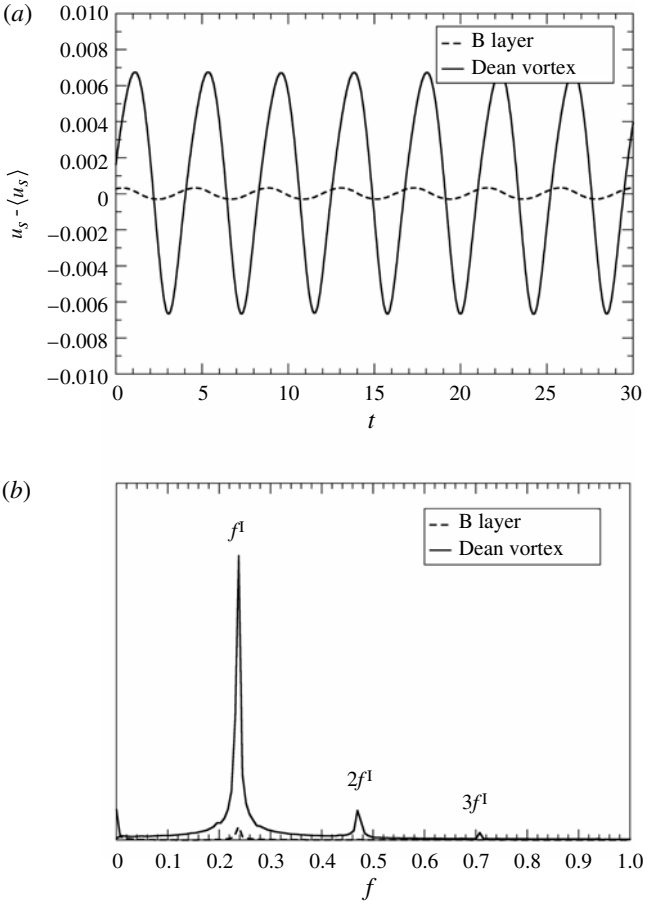

FIGURE 6. Test case D3-P ($Re = 4899, \delta = 0.3$). (*a*) Behaviour of the streamwise velocity fluctuations at two points of the cross-section, located in the Dean vortex region and in the secondary flow boundary, respectively. (*b*) Corresponding velocity power spectra (arbitrary units).

5.2. *Case D3-QP* ($\delta = 0.3, Re = 6128$)

For $\delta = 0.3$ quasi-periodic flow was obtained for Reynolds numbers of 5270, 5562, 5819, 6128, 6594, 7142 and 7850. In particular, detailed results will be illustrated for case D3-QP ($\delta = 0.3, Re = 6128$).

A general overview of the flow unsteadiness can be obtained by considering consecutive maps of the quantity $-Q$ on a generic cross-section (figure 9). Maps are taken at equal dimensionless time intervals of 0.5 starting from an arbitrary instant; during the time interval which separates the last from the first frame the fluid covers, on average, roughly 1/8th of the toroidal length. Non-periodic unsteadiness interests both the Dean vortex regions and the secondary flow boundary layers.

Figure 10(*a*) reports short time samples of the streamwise velocity fluctuations $u_s - \langle u_s \rangle$ at two arbitrary points of the cross-section, located in the upper secondary flow boundary layer and in the upper Dean vortex region, over a dimensionless time interval of 30 starting from an arbitrary instant. The oscillatory non-periodic unsteadiness is clearly visible. Frequency spectra of the same two quantities, taken

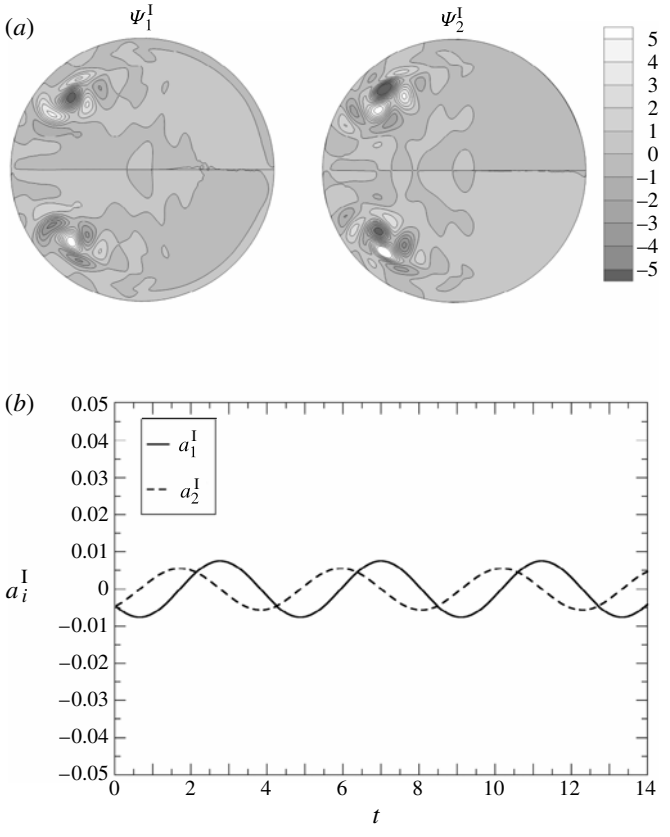

FIGURE 7. Test case D3-P ($Re = 4899, \delta = 0.3$). (*a*) First pair of normalized spatial eigenfunctions for the streamwise velocity u_s, obtained by applying POD to the DNS data. (*b*) Corresponding time-dependent coefficients.

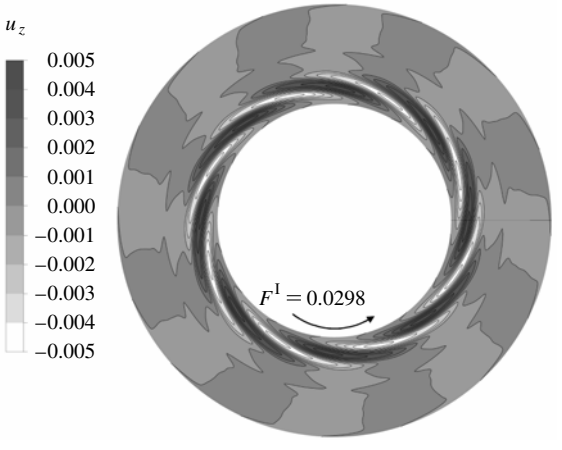

FIGURE 8. Test case D3-P ($Re = 4899, \delta = 0.3$). Instantaneous distribution of the vertical velocity u_z on the equatorial midplane. Directions and angular celerities of the travelling wave are indicated.

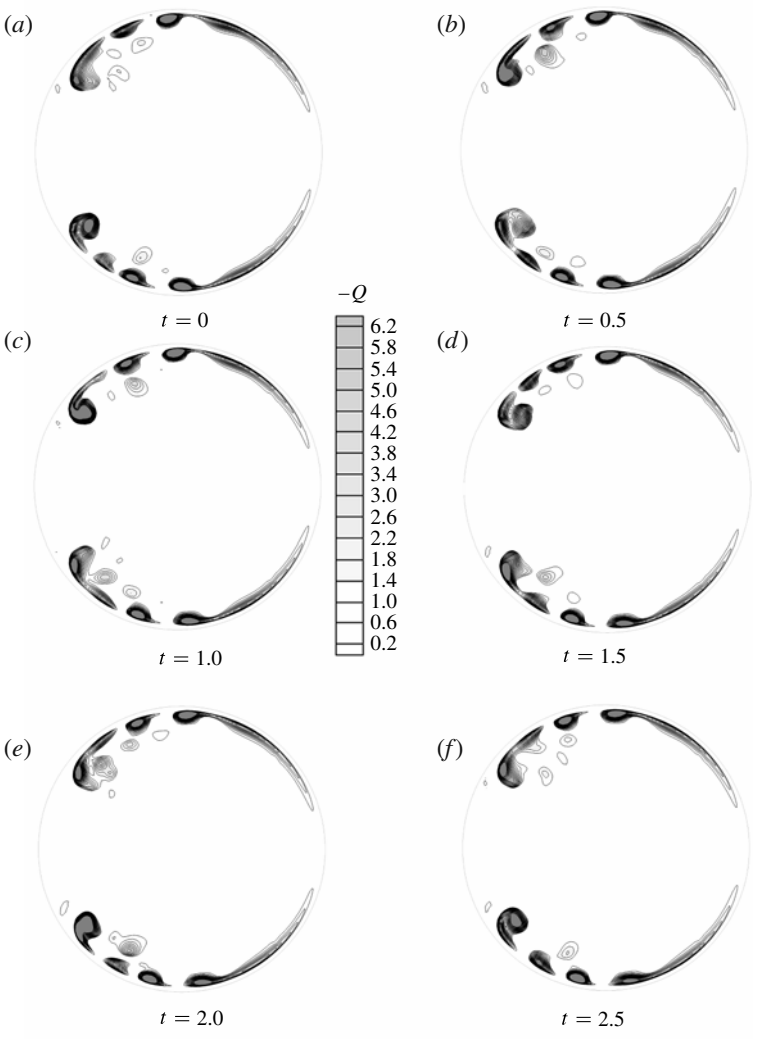

FIGURE 9. Maps of the quantity $-Q$ at dimensionless time intervals of 0.5 starting from an arbitrary instant on a generic cross-section for test case D3-QP ($Re = 6128$, $\delta = 0.3$).

over a dimensionless time interval $\Delta t \approx 220$, are reported in figure 10(*b*). The signals relative to both monitoring locations exhibit sharp peaks at dimensionless frequencies of ~ 0.400 (f^{I}) and ~ 0.165 (f^{II}), while secondary harmonics are very small. Within the present frequency resolution limits $\Delta f = 1/\Delta t \approx 0.005$, the two values 0.165 and 0.400 are totally unrelated and thus must be regarded as two incommensurate frequencies characterizing a quasi-periodic flow. Spectra computed for different points of the flow field and different flow quantities exhibited, in all cases, only the two independent frequencies f^{I}, f^{II} and their first few harmonics.

Modal filtering was applied to the 'raw' time-dependent data in order to separate the two independent modes I and II. The filters G^{I} and G^{II} used are shown in figure 11 and consist of windows of half-width $2\Delta f \approx 0.01$ centred around the corresponding fundamental frequency $f^{\alpha}(\alpha = \mathrm{I}$ or II) and its first two harmonics $2f^{\alpha}$, $3f^{\alpha}$. Further harmonics were practically absent from the data.

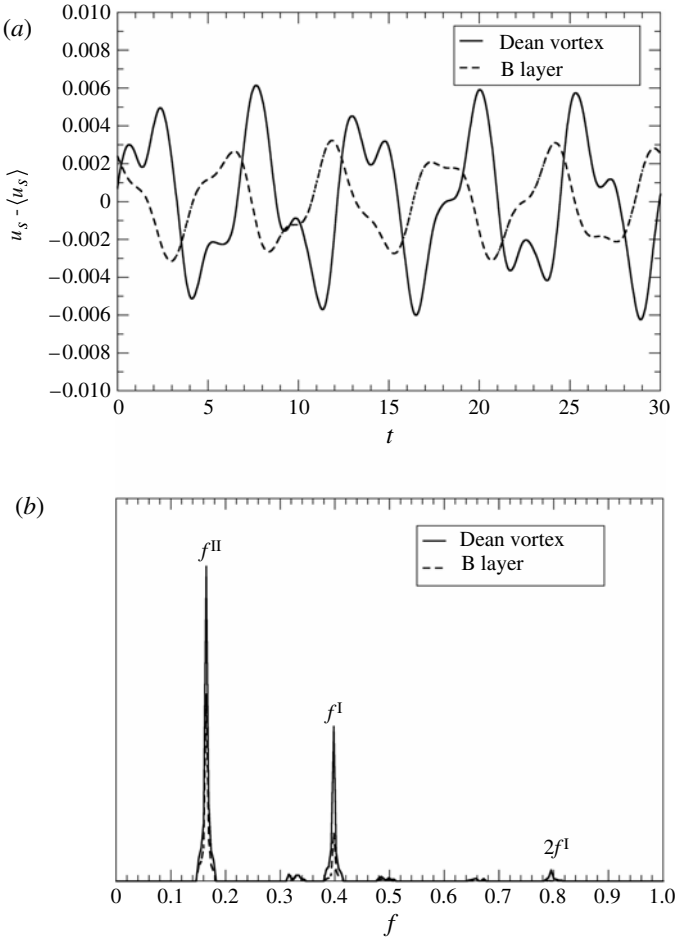

FIGURE 10. Test case D3-QP ($Re = 6128$, $\delta = 0.3$). (*a*) Behaviour of the streamwise velocity fluctuations at two points of the cross-section, located in the Dean vortex region and in the secondary flow boundary, respectively. (*b*) Corresponding velocity power spectra (arbitrary units).

Instead of representing directly the modal components of the flow, which are still time-dependent (periodic), a more synthetic representation can be obtained by using POD decomposition of the two-dimensional cross-section field. It is worth noting that this procedure does not imply a loss of generality because, for a periodic time-dependent field, all the information is contained in the cross-section and the three-dimensional field can be easily reconstructed. The time-averaged flow field is basically identical to that obtained for the same curvature and slightly lower Reynolds numbers in the case of stationary flow (see § 3), and is not reported here for the sake of brevity.

Figure 12(*a*) shows the first two spatial eigenfunctions Ψ_1^{I}, Ψ_2^{I} associated with mode I of the dimensionless streamwise velocity u_s, which have been normalized as described in § 2.4. The first two eigenfunctions capture ∼83 % of the overall variance associated with mode I and, as figure 12(*a*) shows, they are mainly concentrated in the Dean vortex regions. As the single mode characterizing case D3-P, mode I consists of

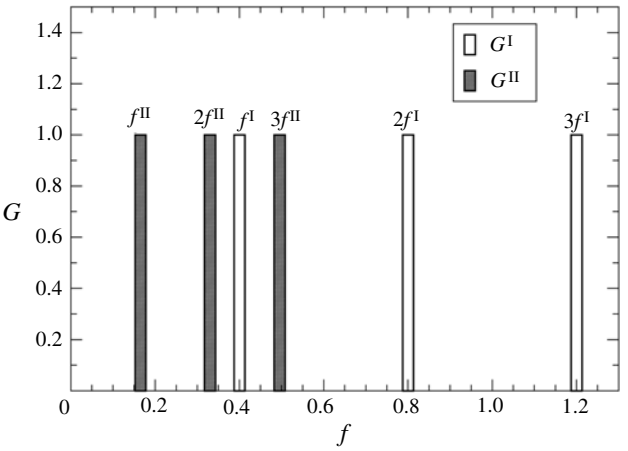

FIGURE 11. Test case D3-QP ($Re = 6128$, $\delta = 0.3$). Filter functions G^{I} and G^{II} used to separate modes I and II.

a varicose travelling wave involving mainly the three-dimensional Dean vortex rings; each spatial eigenfunction Ψ (and therefore the whole mode I) is anti-symmetric with respect to the equatorial midplane, and the varicose patterns associated with the two Dean vortex rings are arranged at any instant in a staggered fashion. The time-dependent coefficients a_1^{I}, a_2^{I} are reported in figure 12(*b*); their amplitude, expressing the intensity of the streamwise velocity fluctuations of frequency f^{I}, is of the order of 2 %.

The spatial structure of mode I is more clearly visible in figure 13(*a*), which reports the instantaneous distribution of the vertical velocity component u_z on the equatorial midplane, where the contribution of mode II is small. This distribution exhibits $k^{I} = 7$ cells and rotates rigidly (or, more exactly, its pure mode I component rotates rigidly) along the torus with a dimensionless rotational celerity $F^{I} = f^{I}/k^{I} \approx 0.057$. The dimensionless linear celerity of the travelling wave, evaluated at the mean radius c, is $2\pi F^{I}/\delta \approx 1.19$. Therefore, the wave celerity is close to the mean fluid velocity so that the wave leads the fluid in the inner (slow-moving) region while it lags behind it in the outer (fast-moving) region. It should be observed that the fundamental frequency f^{I} (0.400) is much larger than the periodic frequency f^{I} of case D3-P (0.238); therefore, the transition from periodic to quasi-periodic flow, with the appearance of the second fundamental frequency f^{II}, is accompanied by a strong increase in the fundamental frequency associated with the varicose modulation of the Dean vortex ring. Since the number of periodic cells along the torus changes only from 8 to 7, this increase in f^{I} is mainly due to a strong increase of the linear wave celerity, from 0.623 to 1.19.

Figure 14(*a*) shows the first two spatial eigenfunctions Ψ_1^{II}, Ψ_2^{II} associated with mode II of the streamwise velocity u_s, while the corresponding time-dependent coefficients a_1^{II}, a_2^{II} are reported in figure 14(*b*). These first two eigenfunctions contain more than 98 % of the overall variance associated with mode II and thus they capture almost completely the spatial shape of the fluctuations possessing the fundamental frequency f^{II}. Fluctuations are localized almost exclusively in the secondary flow boundary layers, while minor amplitudes can be observed in the Dean vortex regions. In the generic cross-section this second mode manifests itself in the form of a pair of vortex sheets which occupy the secondary flow boundary layers and move against

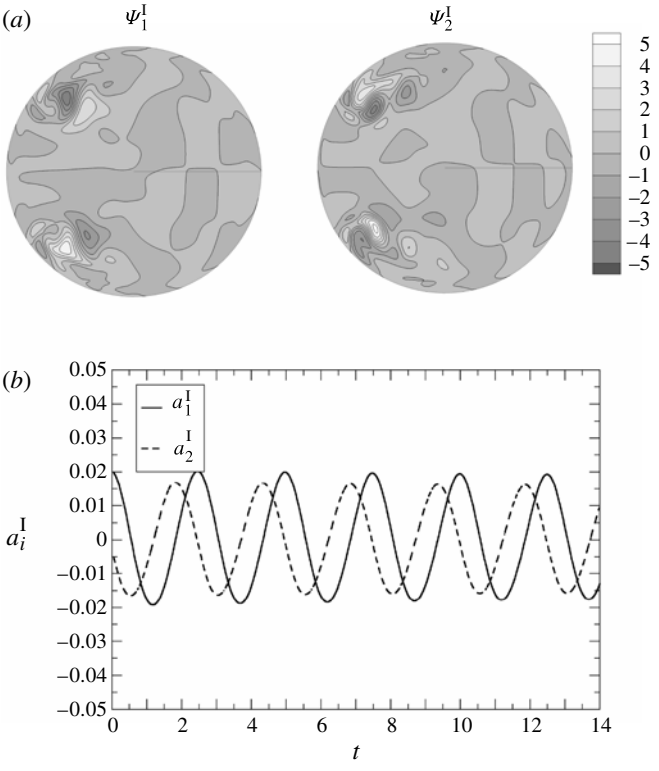

FIGURE 12. Test case D3-QP ($Re = 6128$, $\delta = 0.3$). (*a*) First two pairs of normalized spatial eigenfunctions for mode I of the streamwise velocity u_s, obtained by applying modal filter G^{I} followed by POD to the raw DNS data. (*b*) Corresponding time-dependent coefficients.

the mean secondary flow, from the *I* side towards the *O* side. For this curvature, not only mode I but also mode II (and therefore the whole time-dependent part of the flow field) is anti-symmetric with respect to the equatorial midplane of the torus. The amplitude of the time-dependent coefficients in figure 14(*b*) is of the order of 1.5 % and expresses the intensity of streamwise velocity fluctuations of frequency f^{II}.

The spatial structure of mode-II fluctuations is better shown in figure 13(*b*), which reports the instantaneous distribution of the wall shear stress module on the surface of the toroidal pipe, where the contribution of mode-I oscillations is small. For the present curvature, the distribution exhibits $k^{\mathrm{II}} = 18$ cells and rotates rigidly (or rather, its pure mode-II component does) along the torus with a dimensionless rotational celerity $F^{\mathrm{II}} = f^{\mathrm{II}}/k^{\mathrm{II}} = 0.0092$. The corresponding dimensionless linear celerity at the mean radius c is $2\pi F^{\mathrm{II}}/\delta \approx 0.19$. Therefore, the linear celerity of a mode-II wave is much less than the mean fluid velocity and the linear celerity of a mode-I wave.

An instantaneous, three-dimensional view of Q iso-surfaces for case D3-QP is reported in figure 15. Here, the mode-II travelling wave manifests itself as 18 pairs of oblique, elongated vortical structures while the mode-I wave corresponds to a moderate, 7-cell, streamwise modulation of the twin Dean vortex rings. Although this is not evident from the figure, both the twin arrays of oblique vortices and the streamwise modulations of the Dean vortices are arranged in a staggered fashion with respect to the equatorial midplane. Since modes I and II are actually superimposed,

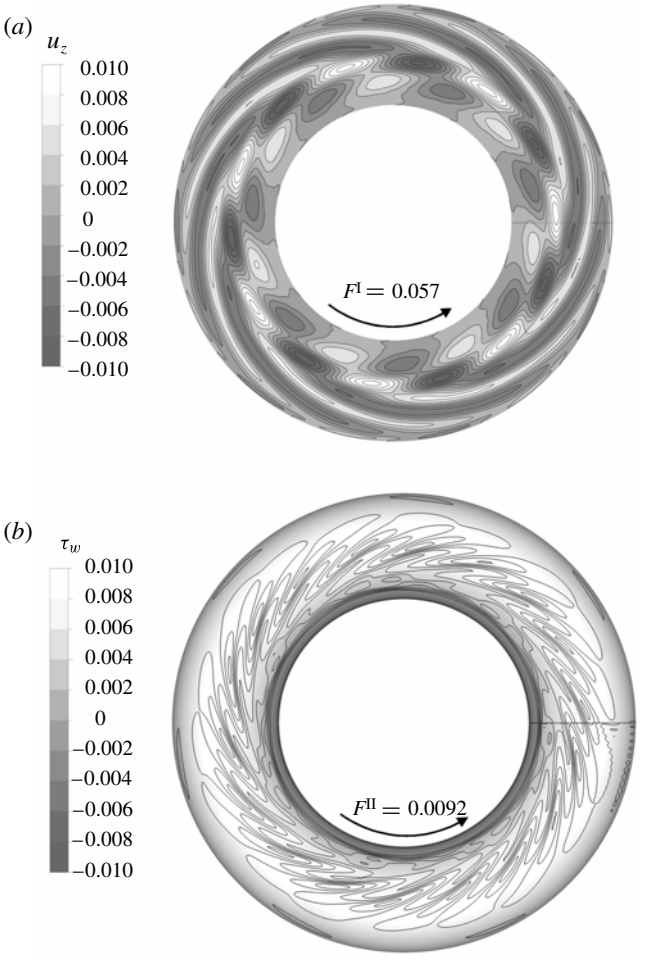

FIGURE 13. Test case D3-QP ($Re = 6128, \delta = 0.3$). (*a*) Instantaneous distribution of the vertical velocity u_z on the equatorial midplane. (*b*) Instantaneous distribution of the wall shear stress on the torus surface. Directions and angular celerities of travelling waves I and II are indicated.

the instantaneous flow structure in figure 15 changes in time as each of its two modal components travels with its own celerity along the torus axis.

Summarizing, the unsteady flow exhibited by test case D3-QP can be described as the superposition of two independent systems of travelling waves. Each system consists of a spatially periodic k-cell pattern (mode) which rotates rigidly around the torus in the same direction as the mean flow with a characteristic rotational celerity F. Conventionally, we denoted by 'mode I' that mainly concentrated in the Dean vortex region. This mode is the less energetic of the two; in space, it appears as a varicose modulation of the Dean vortex rings, while in the cross-section it manifests itself as a pulsatile motion of the Dean vortices. The second mode, conventionally denoted as 'mode II', is mainly concentrated in the secondary flow boundary layers and is the more energetic of the two. In space, this mode consists of two arrays of oblique vortices co-rotating with the Dean ones; in the cross-section, it manifests itself as a pair of vortex trails generated at the edge of the Dean vortices and moving

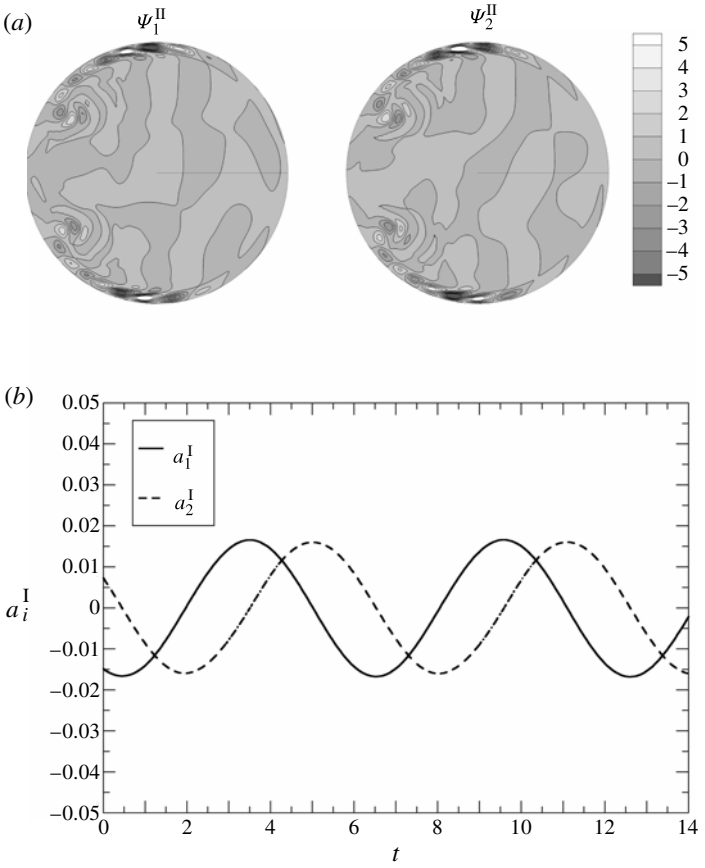

FIGURE 14. Test case D3-QP ($Re = 6128, \delta = 0.3$). (*a*) First pair of normalized spatial eigenfunctions for mode II of the streamwise velocity u_s, obtained by applying modal filter G^{II} followed by POD to the raw DNS data. (*b*) Corresponding time-dependent coefficients.

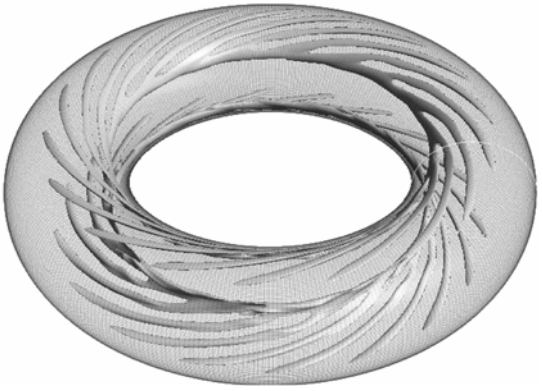

FIGURE 15. Test case D3-QP ($Re = 6128, \delta = 0.3$). Instantaneous isosurface of the quantity Q for $Q = -2.88$. The three-dimensional structure of the oblique travelling wave characterizing mode II is clearly visible.

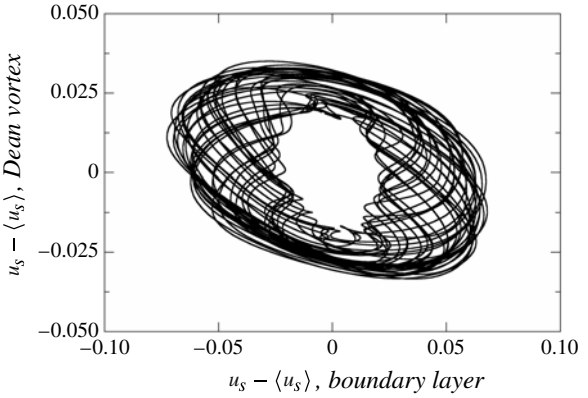

FIGURE 16. Test case D3-QP ($Re = 6128, \delta = 0.3$). Streamwise velocity in a Dean vortex region against streamwise velocity in a secondary flow boundary layer. Time averages have been subtracted from both velocities.

upstream with respect to the mean secondary flow, from the *I* to the *O* side. The whole fluctuating flow field is instantaneously anti-symmetric with respect to the equatorial midplane of the torus.

In the quasi-periodic range examined ($Re = 5270$–7850) the mode-I wavelength number k^{I} decreased from 8 ($Re = 5270$) to 7 ($Re = 5562$ and larger), while the dimensionless mode-I frequency f^{I} increased from 0.275 to 0.400. The mode-II wavelength number k^{II} increased from 10 ($Re = 5270$) to 18 ($Re = 6128$ and larger); the dimensionless mode-II frequency f^{II} increased from 0.035 ($Re = 5270$) to 0.165 ($Re = 6128$) and then decreased slightly for larger Reynolds numbers.

Finally, for the same test case D3-QP ($Re = 6128$, $\delta = 0.3$), figure 16 reports the streamwise velocity in a Dean vortex region against the streamwise velocity in a secondary flow boundary layer over a dimensionless time interval of ∼220. Time averages were subtracted from both velocities. The figure can be regarded as a two-dimensional projection of the system's trajectory in phase space and allows the structure of the quasi-periodic (2-torus) attractor to be appreciated.

5.3. *Case D1-QP* ($\delta = 0.1, Re = 5658$)

As anticipated in § 3, for $\delta = 0.1$ an abrupt transition from steady-state to quasi-periodic flow was observed, in simulations starting from zero-velocity conditions or from a lower-*Re* solution, as soon as the friction Reynolds number exceeded a value of ∼218, corresponding to a bulk Reynolds number of ∼5175. QP solutions were thus computed for $Re = 5208$, 5236, 5400, 5658 and 6280. Detailed results will be presented here for the test case D1-QP characterized by $\delta = 0.1, Re = 5658$.

Figure 17 shows maps of the quantity Q on a generic cross-section of the toroidal pipe. Maps are taken at equal dimensionless time intervals of 0.73 starting from an arbitrary instant; during the time interval which separates the last from the first frame the fluid covers, on average, roughly 1/20th of the toroidal length. Unsteadiness can be observed both in the Dean vortex regions and in the secondary flow boundary layers; at any instant, the flow field is strictly symmetric with respect to the equatorial midplane. As the Q maps suggest, the flow is not periodic in time.

Figure 18(*a*) reports short time samples of the streamwise velocity fluctuations u_s–$\langle u_s \rangle$ at two arbitrary points of the cross-section, located in a secondary flow boundary layer and in a Dean vortex region, over a dimensionless time interval

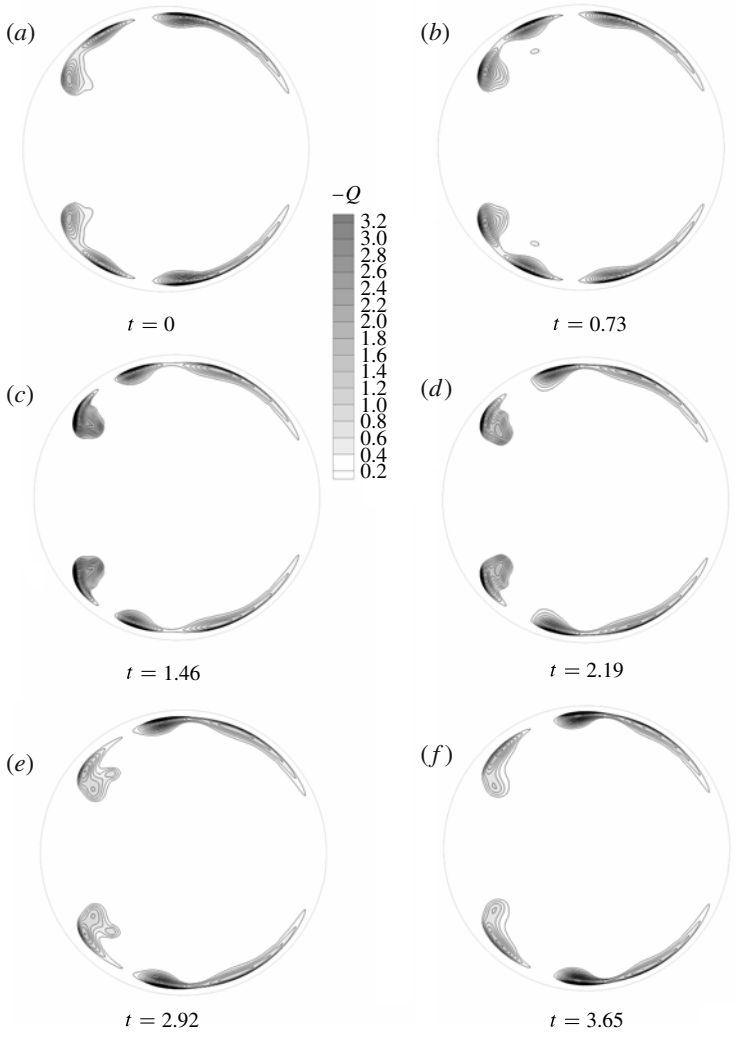

FIGURE 17. Maps of the quantity $-Q$ at dimensionless time intervals of 0.73 starting from an arbitrary instant on a generic cross-section for test case D1-QP ($Re = 5658$, $\delta = 0.1$).

of 30 starting from an arbitrary instant. An oscillatory non-periodic unsteadiness is clearly visible. Frequency spectra of the same two quantities, taken over a much longer dimensionless time interval $\Delta t \approx 130$, are reported in figure 18(*b*). The signal relative to the boundary layer region exhibits a sharp peak at a dimensionless fundamental frequency of ~ 0.20 (f^{II}) and less marked peaks at the harmonic frequencies $2f^{\mathrm{II}} \approx 0.40$ and $3f^{\mathrm{II}} \approx 0.60$ (the reasons for the choice of the I–II nomenclature are the same as for the previous case D3-QP). Shallow peaks are also present at the frequency $f^{\mathrm{I}} \approx 0.27$ and its harmonics $2f^{\mathrm{I}} \approx 0.54$ and $3f^{\mathrm{I}} \approx 0.81$. The signal relative to the Dean vortex region exhibits its highest peak at the frequency $f^{\mathrm{I}} \approx 0.27$, with very shallow secondary peaks at the harmonic frequencies $2f^{\mathrm{I}} \approx 0.54$, $3f^{\mathrm{I}} \approx 0.81$; significant peaks are also present at the frequency f^{II} and its first harmonic frequency $2f^{\mathrm{II}}$. Since, within the present frequency resolution limits $\Delta f = 1/\Delta t \approx 0.007$, the two values 0.20 and 0.27 are totally unrelated, they must be regarded as two incommensurate

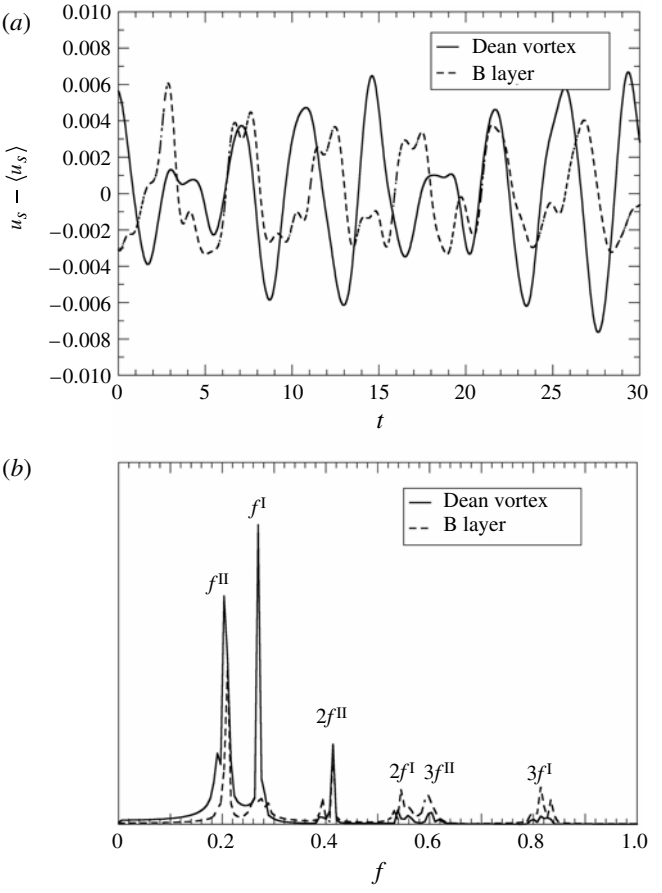

FIGURE 18. Test case D1-QP ($Re = 5658$, $\delta = 0.1$). (*a*) Behaviour of the streamwise velocity fluctuations at two points of the cross-section, located in the Dean vortex region and in the secondary flow boundary, respectively. (*b*) Corresponding velocity power spectra (arbitrary units).

frequencies characterizing a quasi-periodic flow. Spectra for different points of the flow field and different flow quantities exhibited, in all cases, only the two independent frequencies f^{I}, f^{II} and their first few harmonics.

As in case D3-QP, modal filtering was applied to the 'raw' time-dependent quantities computed over the generic cross-section in order to separate the two independent modes I and II from each other and from the time-averaged fields. The filters G^{I} and G^{II} used are similar to those discussed for case D3-QP and shown in figure 11; they consist of windows of half-width $2\Delta f \approx 0.014$ centred around the corresponding fundamental frequency $f^{\alpha}(\alpha = \mathrm{I}$ or II) and its first two harmonics $2f^{\alpha}$, $3f^{\alpha}$ (further harmonics were practically absent from the data). The time-averaged flow field is basically identical to that obtained for a slightly lower Reynolds number in the case of stationary flow (see § 7), and is not reported here for the sake of brevity.

Figure 19(*a*) shows the first two spatial eigenfunctions Ψ_1^{I}, Ψ_2^{I} associated with mode I of the dimensionless streamwise velocity u_s, normalized as described in § 2.4. Time averages have already been removed by the modal filters. These first two eigenfunctions capture more than 83 % of the overall variance associated with

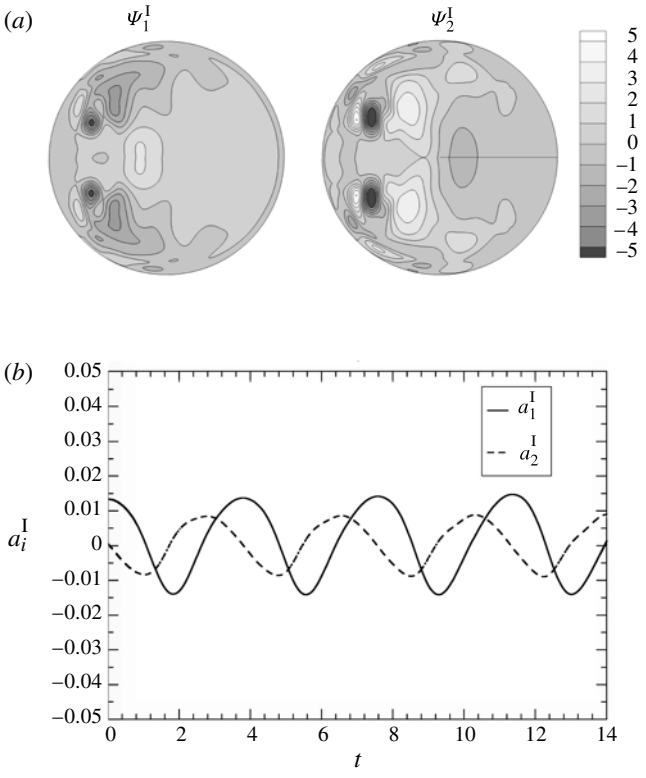

FIGURE 19. Test case D1-QP ($Re = 5658, \delta = 0.1$). (*a*) First pair of normalized spatial eigenfunctions for mode I of the streamwise velocity u_s, obtained by applying modal filter G^{I} followed by POD to the raw DNS data. (*b*) Corresponding time-dependent coefficients.

mode I and thus their distribution can be regarded as a qualitative representation of the spatial shape of the fluctuations of fundamental frequency f^{I}. Figure 19(*a*) shows that they are mainly concentrated in the Dean vortex region. A careful examination of both the primitive flow variables and the associated POD components, also using animations, shows that this mode mainly consists of a couple of travelling waves involving the upper and lower three-dimensional Dean vortices, which preserves at any instant top–bottom symmetry.

The time-dependent coefficients a_1^{I}, a_2^{I} are shown in figure 19(*b*); they can also be interpreted as expressing the *spatial* modulation of the shape functions Ψ along the torus axis. Their amplitude, i.e. the intensity of the streamwise velocity fluctuations of frequency f^{I}, is of the order of 1 %.

The spatial structure of mode I is more clearly visible in figure 20(*a*), which reports the instantaneous distribution in the equatorial midplane of the secondary flow velocity component u_{rp} along the toroidal radius $\hat{r}_p$ defined in § 2.1. Here, the influence of mode II is minor and manifests itself only as a slight departure from exact streamwise periodicity of the pattern shown. This distribution exhibits $k^{\mathrm{I}} = 16$ identical cells; the whole structure (or, more exactly, its pure mode-I component) rotates rigidly along the torus with a dimensionless rotational celerity $F^{\mathrm{I}} = f^{\mathrm{I}}/k^{\mathrm{I}} \approx 0.017$ (number of rotations in the reference time $a/u_{av} = 1/\hat{f}_0$). The dimensionless linear celerity of the travelling wave, evaluated at the mean radius c, is $2\pi F^{\mathrm{I}}/\delta \approx 1.05$. Therefore, the wave celerity

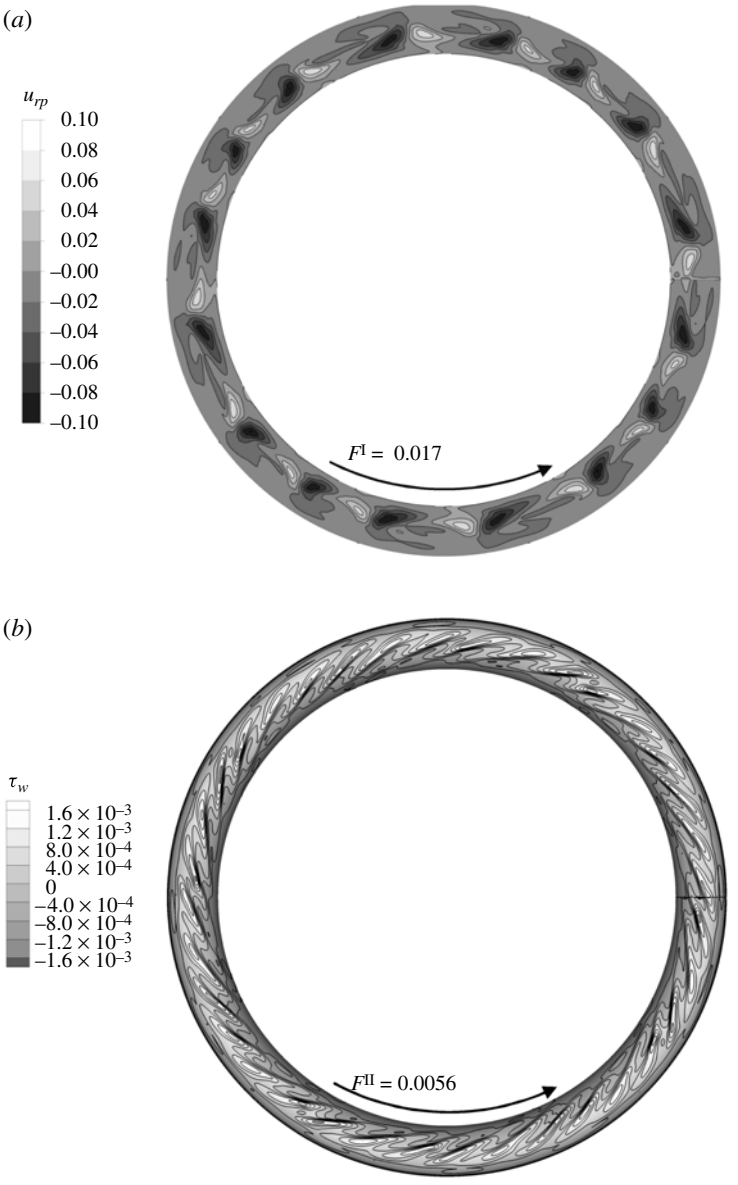

FIGURE 20. Test case D1-QP ($Re = 5658, \delta = 0.1$). (*a*) Instantaneous distribution of the velocity component along the torus radius, u_{rp}, on the equatorial midplane. (*b*) Instantaneous distribution of the wall shear stress module τ_w on the torus surface. Directions and angular celerities of travelling waves I and II are indicated.

is close to the mean fluid velocity and the wave leads the fluid in the inner region while it lags behind it in the outer region. The above values of k^{I} and of the linear celerity are compatible with those reported by Webster & Humphrey (1997) for the lower curvature $\delta = 5.5 \times 10^{-2}$: see § 1.3.

Figure 21(*a*) reports the first two spatial eigenfunctions Ψ_1^{II}, Ψ_2^{II} associated with mode II of the streamwise velocity u_s. These first two eigenfunctions capture more than 95 % of the overall variance associated with mode II and thus, even more than for

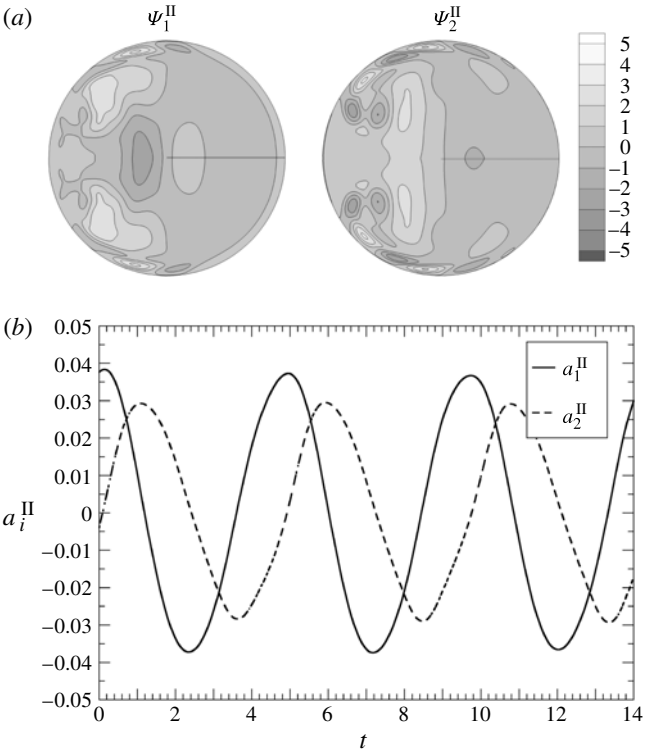

FIGURE 21. Test case D1-QP ($Re = 5658, \delta = 0.1$). (*a*) First pair of normalized spatial eigenfunctions for mode II of the streamwise velocity u_s, obtained by applying modal filter G^{II} followed by POD to the raw DNS data. (*b*) Corresponding time-dependent coefficients.

mode I, they capture the spatial shape of the fluctuations of fundamental frequency f^{II}. Figure 21(*a*) shows that they are mainly concentrated in the secondary flow boundary layers, and particularly near the left (inner) end of these latter. However, significant amplitudes are also present in the Dean vortex regions, which, therefore, exhibit both frequencies f^{I} and f^{II}. A careful examination of the temporal behaviour of the flow shows that, in the generic cross-section, this second mode manifests itself mainly as a pair of vortex sheets which fill the secondary flow boundary layers and move against the mean secondary flow, i.e. from the *I* side towards the *O* side. This is clearly reflected in the sequence of *Q* contours of figure 17. The time-dependent coefficients a_1^{II}, a_2^{II} are reported in figure 21(*b*); their amplitude, which expresses the intensity of the streamwise velocity fluctuations of frequency f^{II}, is of the order of 3–4 %.

The spatial structure of mode II is better shown in figure 20(*b*), which reports the instantaneous distribution of the wall shear stress module on the surface of the toroidal pipe, where the influence of mode I is marginal. This distribution exhibits $k^{II} = 36$ cells; the whole structure (or, more exactly, its pure mode-II component) rotates rigidly along the torus with a dimensionless rotational celerity $F^{II} = f^{II}/k^{II} = 0.0056$. The dimensionless linear celerity of this travelling wave, referred to the mean radius *c*, is $2\pi F^{II}/\delta \approx 0.35$. Therefore, the linear celerity of a mode-II wave is much less than the mean fluid velocity and the linear celerity of a mode-I wave.

Summarizing, the unsteady flow exhibited by test case D1-QP can be described, like in case D3-QP, as the superposition of two independent systems of travelling waves;

unlike in case D3-QP, the fluctuating flow field is instantaneously symmetric with respect to the equatorial midplane of the torus.

All the quasi-periodic cases simulated for the same curvature $\delta = 0.1$, ranging from $Re = 5208$ to 6280, exhibited the same modes and the same number of wavelengths for each mode ($k^{\mathrm{I}} = 16$, $k^{\mathrm{II}} = 36$). The modal frequencies f^{I} and f^{II} varied only negligibly with Re with respect to the values obtained for the reference case D1-QP (0.27 and 0.20, respectively).

As anticipated in § 3, a further QP case was obtained by starting from the solution for case D1-QP ($Re = 5658$) and letting the Reynolds number decrease to ∼4920, well below the critical Reynolds number of ∼5175 for transition to unsteady flow. This case, unattainable 'from below' (i.e. by letting Re increase starting from still fluid or from any lower-Re solution), exhibited the same general features of other quasi-periodic cases, but a reduced number of wavelengths ($k^{\mathrm{I}} = 12$) and a larger dimensionless frequency ($f^{\mathrm{I}} \approx 0.36$) for mode I, while for mode II k^{II} and f^{II} were still 36 and 0.20 as in the other QP cases for $\delta = 0.1$.

5.4. *Case D1-P* ($\delta = 0.1, Re = 4108$)

As anticipated in § 3, using the D1-QP solution ($Re_\tau = 232, Re = 5658$) as initial condition and imposing lower friction Reynolds numbers Re_τ yielded periodic flow (D1-P) at $Re = 4600$, 4108 and 3800 ($Re - Re_c \approx -575, -1067$ and -1375, respectively), well below the critical Reynolds number of ∼5175 for transition to unsteady flow.

In particular, results will be illustrated for the case $Re_\tau = 184$, yielding $Re = 4108 \approx Re_c - 1067$. Figure 22 reports a sequence of contour plots of the quantity $-Q$ on a generic cross-section. The frames are taken at dimensionless time intervals of 0.875, and the sequence covers roughly one period ($1/f^{\mathrm{I}} \approx 4.405$, the dimensionless frequency f^{I} being ∼0.227). The flow symmetry with respect to the equatorial midplane can be appreciated. Near-wall vortices in the upper and lower secondary flow boundary layers are still present, but, unlike in quasi-periodic cases, they now move at the same frequency as the pulsation of the Dean vortices. Note that, in the reference quasi-periodic case D1-QP, the dimensionless modal frequencies f^{I} and f^{II} were ∼0.27 and ∼0.20, respectively slightly above and slightly below the present single frequency. The number of wavelengths in the whole torus is $k^{\mathrm{I}} = 13$, less than that observed for mode I in quasi-periodic flow for Re above the critical value of ∼5175 (5.2), but larger than that observed in quasi-periodic flow for Re below the critical value (2.5). This wavelength number remained unchanged also for the other periodic flow cases simulated as mentioned above ($Re = 4600$ and 3800). It should be mentioned that for the lowest periodic Reynolds number investigated ($Re = 3800 \approx Re_c - 1375$, close to a hypothetical turning point) the flow stabilized itself to $k^{\mathrm{I}} = 13$ only after a long transient in which the wavelength number changed erratically between 12 and 13.

5.5. *Instability mechanisms*

Only a few authors so far have described transitional unsteady regimes occurring between stationary and turbulent flow in curved pipes; among them Sreenivasan & Strykowski (1983) for $\delta \approx 0.058$ and Webster & Humphrey (1997) for $\delta \approx 0.055$. However, the former authors gave only a qualitative description of the ensuing unsteady flow, while the latter described it as time-periodic and identified a single travelling wave. Hüttl & Friedrich (2001), for $\delta = 0.1$, predicted unsteady flow in the same range of Reynolds number but gave only a statistical description of the results without specifying the nature of the unsteadiness. All the above studies agree on the

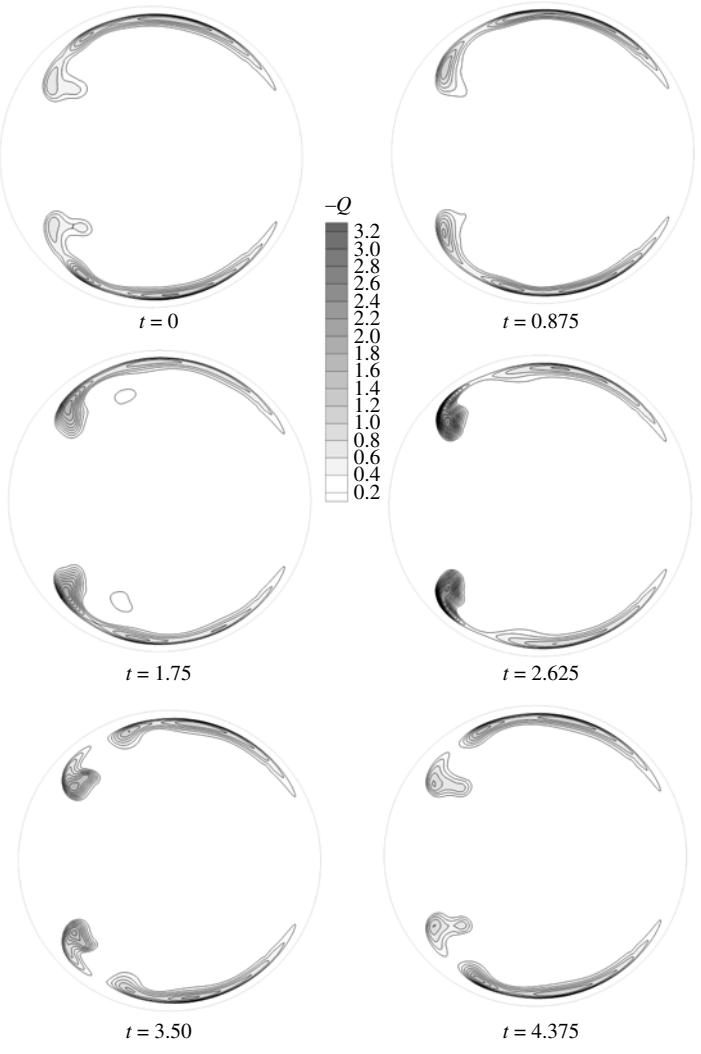

FIGURE 22. Maps of the quantity $-Q$ at dimensionless time intervals of 0.875 starting from an arbitrary instant on a generic cross-section for test case D1-P ($Re = 4108$, $\delta = 0.1$).

fact that the loss of stability of the Dean flow occurs for $Re \approx 5000$, much lower than the values predicted by all correlations in § 1.3 as the critical ones for transition to turbulence proper.

The present results show that what happens at $Re \approx 5000$ is a loss of stability of the base steady-state flow in favour of an oscillatory, P or QP, flow. The details of this transition depend on the curvature δ. Transition to chaotic flow proper (turbulence) occurs only at far larger $Re(\sim 8000)$.

The experimental identification of oscillatory (periodic and quasi-periodic) flows has played a central role in the understanding of transition to turbulence (Fenstermacher *et al.* 1979; Gollub & Benson 1980). In fully three-dimensional flows permanent oscillating solutions (either periodic or quasi-periodic) have been documented only in configurations involving non-uniform body forces, such as those caused by buoyancy (Fusegi, Hyun & Kuwahara 1992) or rotation (Knightly & Sather 1993). Recently,

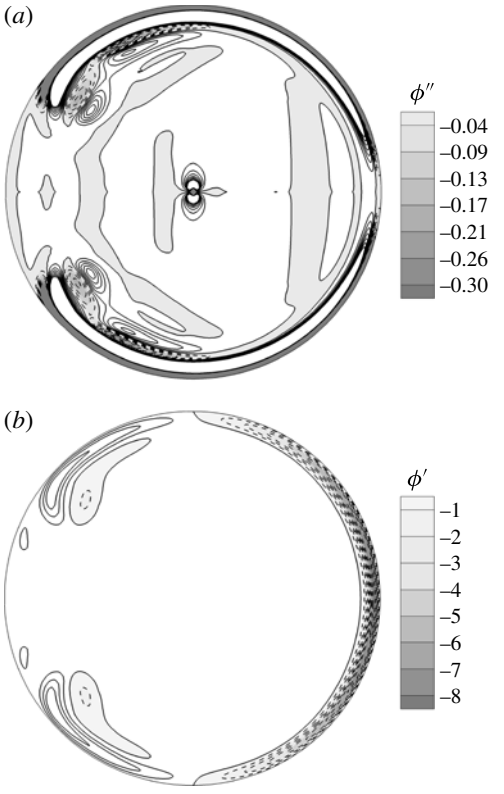

FIGURE 23. Test case D3-QP ($Re = 6128, \delta = 0.3$). Cross-sectional maps of (*a*) Rayleigh discriminant ϕ'', (5.1), computed from the time-averaged secondary flow field, (*b*) Rayleigh discriminant ϕ', (5.2), computed from the time-averaged streamwise flow field. Stable regions ($\phi > 0$) are shown in white with solid contour lines, unstable regions ($\phi < 0$) in grey with dashed contour lines.

travelling waves in channel flow have received considerable attention for their potential role in transition to turbulence (Kerswell 2005); in straight channels, they are unstable and thus cannot persist indefinitely, while in the present, curved pipe, configuration they appear to be stabilized by the centrifugal forces.

As regards the mechanism of the unsteadiness in curved pipes, Webster & Humphrey (1997) suggested that it is a centrifugal instability of the secondary (cross-) flow rather than an instability of the main (streamwise) flow. When applied to the secondary flow in the cross-section of the toroidal pipe, the Rayleigh discriminant in (1.7) must be written as

$$\phi'' = \frac{1}{r^3}\frac{\partial}{\partial r}(ru_\theta)^2, \tag{5.1}$$

in which u_θ is the azimuthal (circumferential) velocity of the secondary flow and r is the distance from the centre of the cross-section. A map of ϕ'' on the generic cross-section for case D3-QP, based on the time-averaged secondary flow field, is reported in figure 23(*a*). Note that, since the flow is not centro-symmetric, (5.1) makes ϕ'' diverge at the origin and clearly is not applicable there. The secondary flow boundary layers

appear as stable areas surrounded on either side by unstable regions, which seems to support the interpretation proposed by Webster & Humphrey.

However, a strong argument against this interpretation is that, if it were true, the onset of instability should be associated with a certain critical value of the Dean number $De = Re\sqrt{\delta}$, which controls the intensity of the secondary flow, and not of the Reynolds number. Webster & Humphrey (1997) considered a single value of the curvature and thus could not analyse the independent effects of these two quantities. In our simulations, however, the onset of unsteadiness is predicted to occur at a Reynolds number between 4556 and 4605 ($De = 2495$–2552) for $\delta = 0.3$, and at a Reynolds number between 5139 and 5208 ($De = 1625$–1642) for $\delta = 0.1$, which shows that it is mainly controlled by Re rather than by De. In other words, geometry D3 sustains a stationary Dean flow in the presence of a secondary circulation much more intense than that supposedly causing unsteadiness in the lower curvature geometry D1.

On the other hand, following the suggestion of Sreenivasan & Strykowski (1983), the Rayleigh criterion should be applied to the main flow in the toroidal pipe. In this case, the appropriate form of the Rayleigh discriminant in (1.7) is

$$\phi' = \frac{1}{r_p^3}\frac{\partial}{\partial r_p}(r_p u_s)^2, \tag{5.2}$$

in which u_s is the streamwise velocity and r_p is the normal distance from the axis of the torus. A map of ϕ' on the generic cross-section for case D3-QP, based on the time-averaged flow field, is reported in figure 23(*b*). It shows two main regions of centrifugal (Rayleigh) instability, one located near the outer wall and one corresponding to the Dean vortices, where ϕ' is much more negative than ϕ''. While a near-wall negative Rayleigh discriminant does not necessarily imply flow unsteadiness, due to the stabilizing effect of viscous forces, the Dean vortex regions are likely candidates for the locus of origin of the first instability that leads to the transition from stationary to unsteady flow. This fact, together with the independence of the critical Reynolds number from the curvature δ, supports the view that the transition from stationary to unsteady regimes is driven by a centrifugal instability of the main (streamwise) flow, and not of the secondary flow.

However, it must be observed that the strongly negative ϕ' region in figure 23(*b*) in the proximity of the Dean vortex is associated with the 'kink' in the distribution of the streamwise velocity u_s clearly visible, for example, in figure 4(*a*) and caused by the convective transport of u_s by the secondary flow. Thus, although indirectly, the secondary circulation does play a crucial role in determining the centrifugal instability of the main flow, which supports the view that main and secondary flow should not be probed separately for stability. Note that the same 'kink' is associated with a relative minimum (implying two inflection points) in the radial profiles of the streamwise velocity, which may also be a potential instability source. Thus, different criteria basically converge in pointing to the 'kink' region as the locus for the onset of oscillatory instability in the basic steady flow.

The present problem exhibits obvious analogies, but also some relevant differences, with respect to the much more studied Taylor–Couette flow. In both cases a stationary vortex flow pattern (Dean vortices versus Taylor vortices) is destroyed by centrifugal instabilities in favour of an unsteady flow as a critical value of a control parameter is exceeded. However, in the Taylor–Couette problem the full supercritical bifurcation sequence from stationary to periodic and then to quasi-periodic flow is observed (Fenstermacher *et al.* 1979), whereas in the present toroidal pipe problem this is true

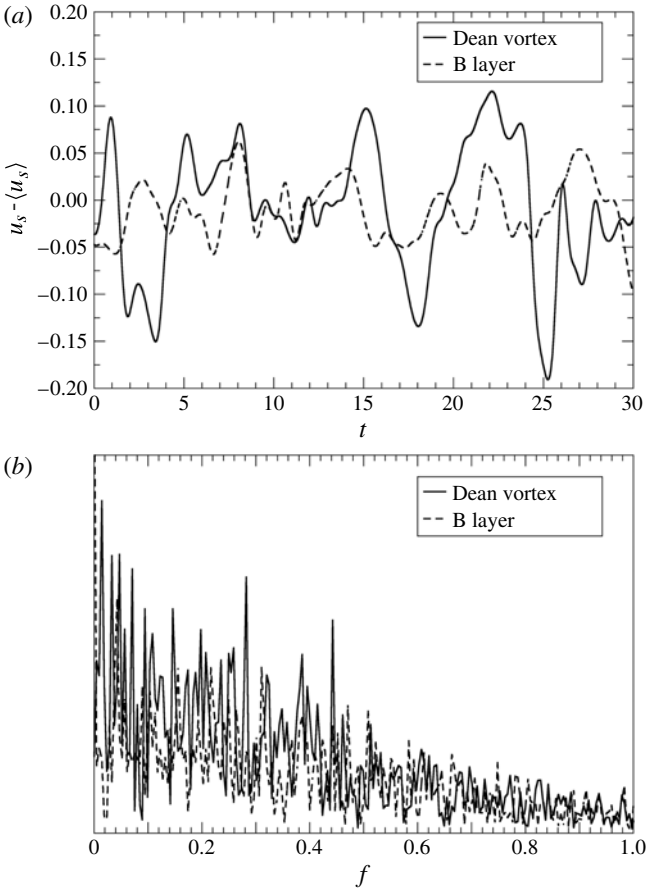

FIGURE 24. Test case D3-C ($Re = 8160$, $\delta = 0.3$). (*a*) Behaviour of the streamwise velocity fluctuations at two points of the cross-section, located in the Dean vortex region and in the secondary flow boundary, respectively. (*b*) Corresponding velocity power spectra (arbitrary units).

for high curvatures ($\delta = 0.3$) but not for low curvatures ($\delta = 0.1$), where a subcritical bifurcation scenario seems to prevail.

6. Chaotic flow

The highest Reynolds numbers for which clearly quasi-periodic solutions were obtained were 7859 ($\delta = 0.3$) and 6280 ($\delta = 0.1$). For the higher curvature ($\delta = 0.3$), a moderate increase of Re to 8160 was sufficient to yield a clearly chaotic solution. For $\delta = 0.1$, Reynolds numbers in the range ∼6500–8000 gave rise to long and erratic transients while clearly chaotic solutions were obtained only for $Re >$ ∼8000. For both curvatures, results will be presented for a Reynolds number of 8160 (cases D3-C and D1-C).

6.1. *Case D3-C* ($\delta = 0.3, Re = 8160$)

Figure 24(*a*) reports short time samples of the streamwise velocity fluctuations u_s–$\langle u_s \rangle$ at two arbitrary points of the cross-section, located in the secondary flow boundary layer and in the Dean vortex region. Both the location of the monitoring points and

the dimensionless duration of the sample (30 units) are the same as in figure 10(*a*), relative to case D3-QP. Frequency spectra of the two velocities, taken over a time interval $\Delta t \approx 200$, are reported in figure 24(*b*). For both locations, spectra exhibit an almost continuous distribution of frequencies, characteristic of highly chaotic flow. Although some peaks stand out on the broadband background, there is no clear residual of the modal frequencies ($f^{\mathrm{I}} \approx 0.4$, $f^{\mathrm{II}} \approx 0.165$) observed in the corresponding quasi-periodic case D3-QP: see figure 10(*b*). Similar broadband spectra are obtained for different points of the flow field and different flow quantities.

For this case, the numerical simulation conducted starting from zero-velocity conditions initially yielded a quasi-periodic flow, similar to that predicted for lower Reynolds numbers. However, at a certain instant an instability of the outer region manifested itself in the form of irregular vortices which were rapidly swept by the cross-flow into the secondary boundary layers, where they destroyed the regular vortex pattern characteristic of QP flows. Subsequently, the irregularities propagated to the Dean vortex regions until a chaotic flow condition was attained in the whole cross-section. Figure 25 illustrates the initial stages of this sequence by reporting maps of the quantity $-Q$ on an arbitrary cross-section at dimensionless time intervals of 1.32, starting from the first appearance of the outer layer instability. Note that the vortex trails in the secondary boundary layers, associated with mode II in QP flows, continue to exist also in the present chaotic flow conditions, although they lose any periodicity and regularity; also, the Dean vortices continue to exist as permanent flow structures, but their pulsatile motion becomes aperiodic and the phase shift between the upper and lower half-channels is not clearly identifiable any more.

These results show that, for this high curvature ($\delta = 0.3$), the centrifugal instability of the main flow in the outer region appears to be the mechanism causing the loss of stability of the quasi-periodic solution prevailing at lower Reynolds numbers.

The time-averaged secondary flow in the cross-section is not illustrated here since, once made dimensionless by the average streamwise velocity, it is almost indistinguishable from that obtained for stationary flow, e.g. case D3-S in figure 4(*d*). This shows that flow unsteadiness, either of regular or chaotic nature, does not significantly affect the time-mean flow: for a given curvature, as the Reynolds number increases, the Dean circulation attains rather early (well within the stationary range) an asymptotic shape and a dimensionless intensity which are little affected (on average) by the subsequent transitions to unsteady and chaotic behaviour.

A map of the root mean square values of the velocity fluctuations along the streamwise direction for case D3-C is reported in figure 26(*a*). The outer region has a high level of fluctuations and is the most unsteady. Fluctuations in this region were almost completely absent in the quasi-periodic case D3-QP, and thus appear to be purely chaotic.

A further increase of Re does not change the overall flow structure: figure 26(*b*) reports the r.m.s. streamwise fluctuation for $Re = 13\,180$, and exhibits no relevant difference with respect to case D3-C in the distribution and dimensionless intensity of turbulence.

6.2. *Case D1-C* ($\delta = 0.1, Re = 8160$)

Figure 27(*a*) reports short time samples of the streamwise velocity fluctuations $u_s - \langle u_s \rangle$ at two arbitrary points of the cross-section, located in the secondary flow boundary layer and in the Dean vortex region. Both the location of the monitoring points and the dimensionless duration of the sample (30 units) are the same as in figure 18(*a*), which is for case D1-QP. The time series in figures 17(*a*) and 25(*a*) do not show any obvious

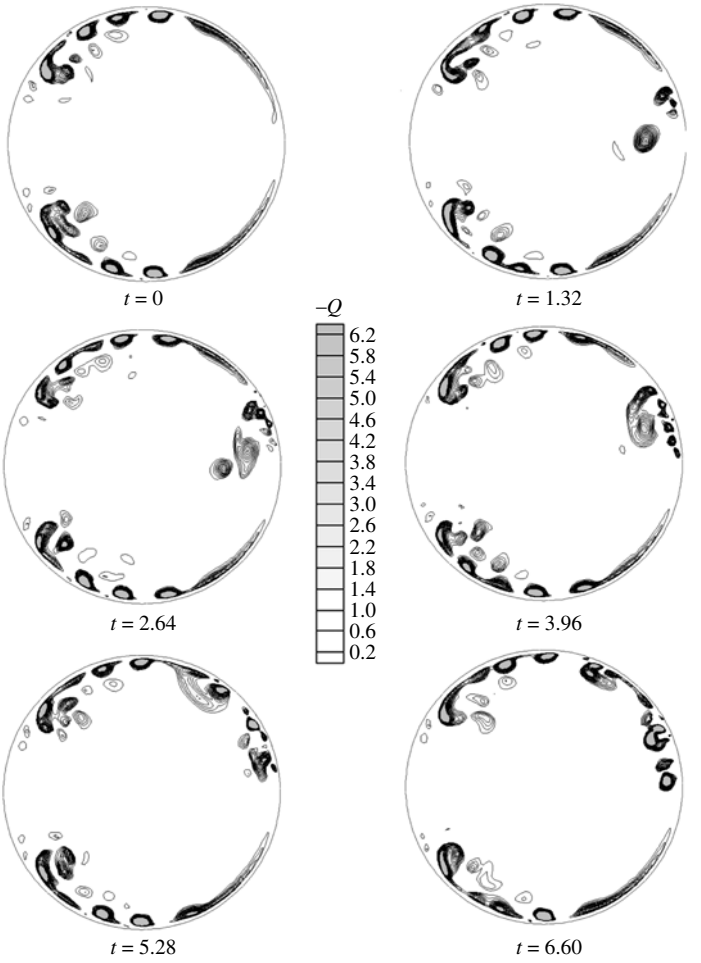

FIGURE 25. Test case D3-C ($Re = 8160, \delta = 0.3$). Maps of the quantity $-Q$ on a generic cross-section at dimensionless time intervals of 1.32, starting from the onset of instability in the outer layer.

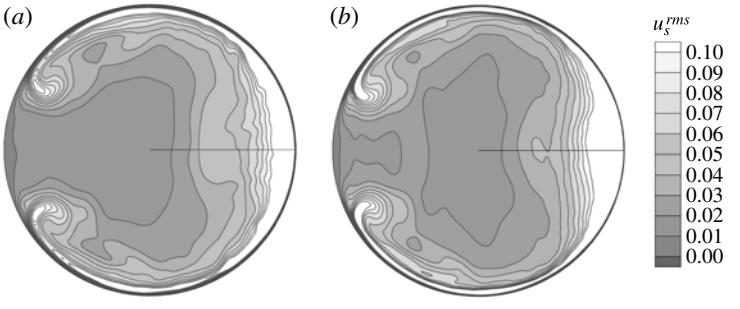

FIGURE 26. Streamwise root mean square velocity fluctuations for chaotic flow and $\delta = 0.3$. (*a*) $Re = 8160$, (*b*) $Re = 13\,180$.

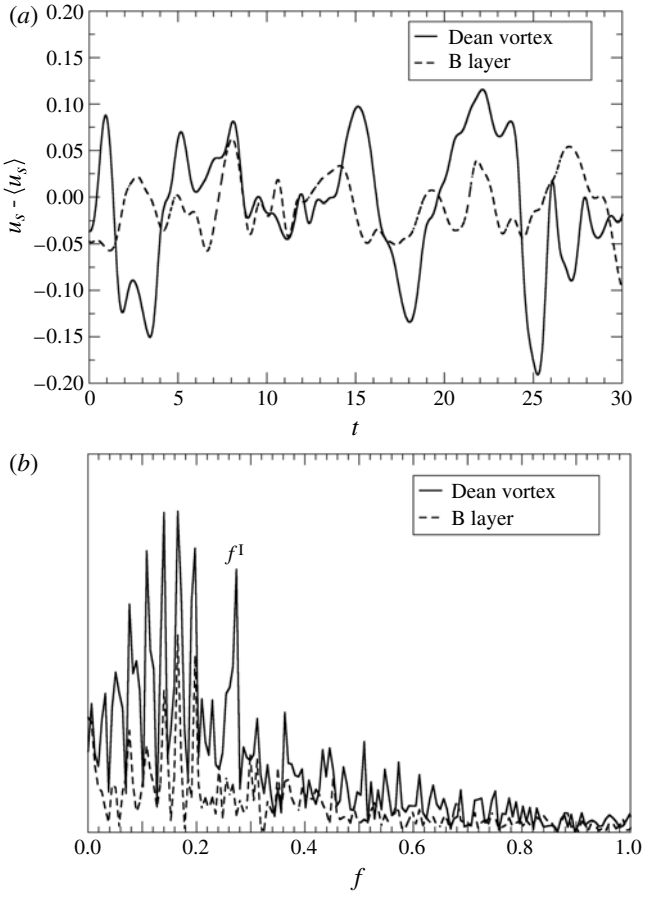

FIGURE 27. Test case D1-C ($Re = 8160$, $\delta = 0.1$). (*a*) Behaviour of the streamwise velocity fluctuations at two points of the cross-section, located in the Dean vortex region and in the secondary flow boundary, respectively. (*b*) Corresponding velocity power spectra (arbitrary units).

differences; however, the corresponding power spectra are completely different; see parts (*b*) of these figures. For case D1-C, figure 27(*b*), the spectra for both monitoring points, taken over a time interval $\Delta t \approx 200$, exhibit a large number of peaks occurring at incommensurate frequencies, which is a clear indication of chaotic flow. In the spectrum relative to the Dean vortex, but not in that relative to the boundary layer region, the spectral peak corresponding to the frequency $f^{I} \approx 0.27$ of the mode-I travelling wave (varicose instability of the Dean vortex ring) is still recognizable. The cluster of frequencies observed in the spectra relative to both monitoring points in the interval $\sim$0.1–0.2 replaces the single frequency $f^{II} \approx 0.2$ of mode II (oblique vortex trail in the boundary layer region) and corresponds to a low-frequency, non-sinusoidal amplitude modulation of the mode-II vortices.

Spectra obtained for different points of the flow field and different flow quantities exhibit the same overall chaotic behaviour.

Figure 28 reports the instantaneous map of the quantity $-Q$ on a cross-section at an arbitrary time. When compared to the similar maps reported for the quasi-periodic case D1-QP in figure 17, the present distribution exhibits a loss of instantaneous symmetry

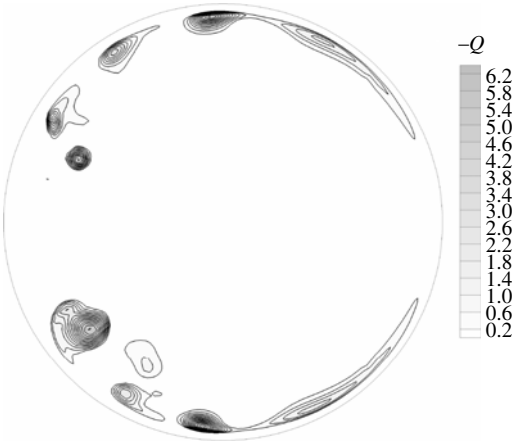

FIGURE 28. Instantaneous map of the quantity $-Q$ on a generic cross-section for test case D1-C ($Re = 8160$, $\delta = 0.1$).

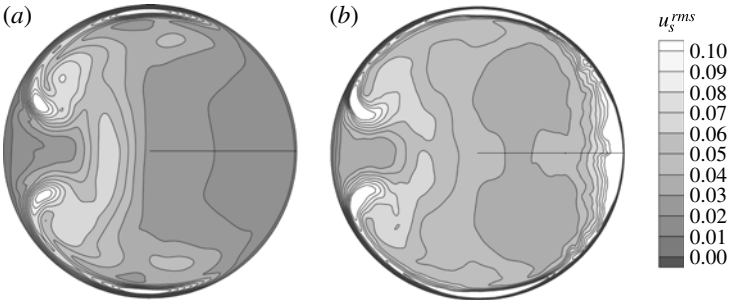

FIGURE 29. Streamwise root mean square velocity fluctuations for chaotic flow and $\delta = 0.1$. (*a*) $Re = 8160$, (*b*) $Re = 14\,700$.

with respect to the equatorial midplane of the torus and a larger irregularity of the secondary flow in the Dean vortex region. The outer flow region remains basically stationary as in case D1-QP.

The time-averaged secondary flow in the cross-section is very similar (once made dimensionless by the average streamwise velocity) to the secondary flow predicted for the stationary case D1-S and shown in figure 4(*b*). Therefore, it is not illustrated here.

A map of the root mean square velocity fluctuation along the streamwise direction for case D1-C is reported in figure 29(*a*). Of course, fluctuations include all the spectral components in figure 27(*b*), i.e. both chaotic fluctuations proper and what is left of the low-frequency, quasi-periodic oscillations. Figure 29(*a*) shows that high values of the streamwise fluctuation are attained both in the Dean vortex regions and in the secondary flow boundary layers for $\theta \approx 0$ or π, while the outer region is basically stationary despite the overall chaotic nature of the solution. This suggests that the centrifugal instability of the main flow in this region has not yet manifested itself at the present Reynolds number of 8160.

Quite a different picture is obtained if the Reynolds number is further increased: figure 29(*b*) reports the r.m.s. streamwise fluctuation for a higher Re(14 700), well into the turbulent range. In this case, fluctuations attain high values not only in the regions

mentioned for the lower-Re case, but also near the outer wall, which shows that the centrifugal instability of the main flow in this region has occurred at some Reynolds number intermediate between 8160 and 14 700. Since the spatial resolution criteria for DNS discussed in § 2.2 are not fully satisfied by the computational mesh for this latter value of Re, the corresponding case will not be analysed in detail here and is reported only for the purpose of comparison with the early-chaotic case D1-C.

7. Summary and conclusions

Albeit limited to two values of the curvature, the present study has revealed a rich variety of phenomena in the transition to turbulence in toroidal pipes.

A supercritical transition from stationary to periodic flow was observed only for the higher curvature $\delta = 0.3$ and occurred for a Reynolds number intermediate between 4556 and 4605. The resulting flow was characterized by a travelling wave affecting mainly the Dean vortex region and taking the form of a varicose modulation of the twin Dean vortex rings, which, in the whole periodic range of Reynolds numbers, included $k^{\mathrm{I}} = 8$ cells (wavelengths) along the axis of the torus and was instantaneously anti-symmetric with respect to its equatorial midplane. Still for $\delta = 0.3$, the further transition to quasi-periodic flow, characterized by two independent fundamental frequencies f^{I} and f^{II} and by their first few harmonics, occurred for Re between 5042 and 5270. The two frequencies were associated with distinct travelling waves, the first affecting mainly the Dean vortex rings and taking the form of a varicose modulation, the second affecting mainly the secondary flow boundary layers and manifesting itself as an array of oblique vortices produced at the edge of the Dean cells, co-rotating with these latter and travelling from the inner towards the outer side, i.e. against the secondary circulation. In the Reynolds number range for which a quasi-periodic regime existed, the number k^{I} of mode-I wavelengths in the whole torus decreased from 8 to 7 while the number k^{II} of mode-II wavelengths increased from 10 to 18.

For the lower curvature $\delta = 0.1$, the present computational results indicate the existence of a subcritical Hopf bifurcation at a Reynolds number Re_c close to 5175 and of a secondary Hopf bifurcation to quasi-periodic flow at a lower Reynolds number close to 4900. Starting from zero-velocity initial conditions, steady-state flow remained stable up to a Reynolds number of 5139, while a further increase in Re to 5208 led to a quasi-periodic flow which remained stable up to $Re = 6280$ or larger, and was characterized in this whole range by $k^{\mathrm{I}} = 16$, $k^{\mathrm{II}} = 36$ with dimensionless modal frequencies f^{I}, f^{II} of $\sim$0.27 and $\sim$0.20, respectively. When a quasi-periodic solution (namely, that obtained for case D1-QP at $Re = 5658$) was used as the initial condition, it was possible to obtain a further, stable, quasi-periodic solution for a Reynolds number well below the critical (Hopf) value of $\sim$5175. In particular, the QP solution at $Re = 4920$ was characterized by $k^{\mathrm{I}} = 12$, $k^{\mathrm{II}} = 36$ and by dimensionless modal frequencies f^{I}, f^{II} of $\sim$0.36 and $\sim$0.21, respectively. A further decrease of the imposed driving force starting from the same (QP) initial conditions led to the disappearance of mode II and to a stable periodic solution at $Re = 4108$, characterized by $k^{\mathrm{I}} = 13$, $f^{\mathrm{I}} = 0.227$. With this 'backward' procedure, steady-state flow was obtained only when the Reynolds number was reduced to values well below 4000 (in particular, a test case was computed for $Re = 3490$). All the periodic and quasi-periodic solutions obtained for $\delta = 0.1$ exhibited instantaneous symmetry about the equatorial midplane.

An analysis based on the application of Rayleigh's centrifugal stability criterion suggested that for both curvatures the occurrence of unsteady modes was triggered by a centrifugal instability of the main flow located in the Dean vortex region, rather

than by a centrifugal instability of the cross- (secondary) flow as suggested by other authors.

Also, the further transition from quasi-periodic to chaotic flow occurs with different mechanisms for the two curvatures.

For the high-curvature case ($\delta = 0.3$), convergence to quasi-periodic flow is obtained in the whole Reynolds number range 5270–7850. As Re increases slightly beyond this value ($Re = 8160$), strong fluctuations, associated with random streamwise vortices, arise in the outer region. The statistically stationary flow regime that ensues is characterized by a broadband, almost continuous, spectrum of frequencies in which the quasi-periodic modal frequencies f^{I} and f^{II} are not recognizable any longer. A further increase of the Reynolds number to 13 180 does not modify to any appreciable extent the flow regime and the distribution of the velocity fluctuations. This phenomenology suggests that, at high curvatures, the abrupt breakdown of the quasi-periodic flow is associated with the occurrence of a centrifugal instability of the main flow, located in the outer region of the pipe.

In the case $\delta = 0.1$, the convergence of the results to quasi-periodic flow obtained for Reynolds numbers between 5208 and 6280 becomes impossible to achieve as the Reynolds number increases beyond the latter value, and is replaced by long and erratic transients. For $Re = 8160$, the solution, albeit stationary in a statistical sense, exhibits a large number of frequencies. The characteristic frequency f^{I}, associated with the varicose, symmetric modulation of the Dean vortex rings is still recognizable in power spectra, whereas the frequency f^{II} is replaced by a cluster of nearby frequencies, associated with an amplitude modulation of the mode-II structures (travelling vortices in the secondary flow boundary layers). At this Reynolds number, the outer region is basically stationary. Only when the Reynolds number increases further does the outer region become unsteady and characterized by an irregular production of streamwise vortices, which are then transported by the cross-flow and destroy all remains of regular oscillations. This behaviour suggests that, at sufficiently low curvature, the gradual breakdown of the regular, quasi-periodic flow may result from nonlinear interactions between modes I and II. Only at higher Re does the centrifugal instability of the main flow in the outer region of the pipe manifest itself and turn the flow pattern into one characterized by strong fluctuations, not only in the Dean vortex and cross-flow boundary layer regions but also in the outer region.

On the basis of the present simulations, of results from the literature, and of asymptotic arguments, a tentative flow regime map in the Re–δ plane can be sketched as in figure 30. This takes into account the present results for $\delta = 0.3$ and 0.1, the (qualitative) experimental findings of Sreenivasan & Strykowski (1983) for $\delta = 0.058$, and the experimental results of Webster & Humphrey (1997) for $\delta = 0.055$. Here we assumed that the oscillatory flow regimes described by the above authors as periodic are actually instances of quasi-periodic flow. Moreover, the map takes account of the fact that, for $\delta = 0$ (straight pipe), a direct transition from stationary laminar to turbulent (chaotic) flow occurs.

The solid lines in figure 30 denote transitions for increasing Re, while the dashed lines correspond to transitions for decreasing Re. The regions indicated as P-BW and QP-BW are attainable only by letting the Reynolds number decrease from initial conditions corresponding to a higher-Re solution.

Schematic bifurcation diagrams corresponding to different intervals of δ are drawn in the lower part of the figure; in the regions close to $\delta = 0.3$ and $\delta = 0.1$ they are qualitatively identical to those reported in figures 3(*a*) and 3(*b*), respectively. H denotes a Hopf bifurcation from stationary to periodic flow while H2 denotes a

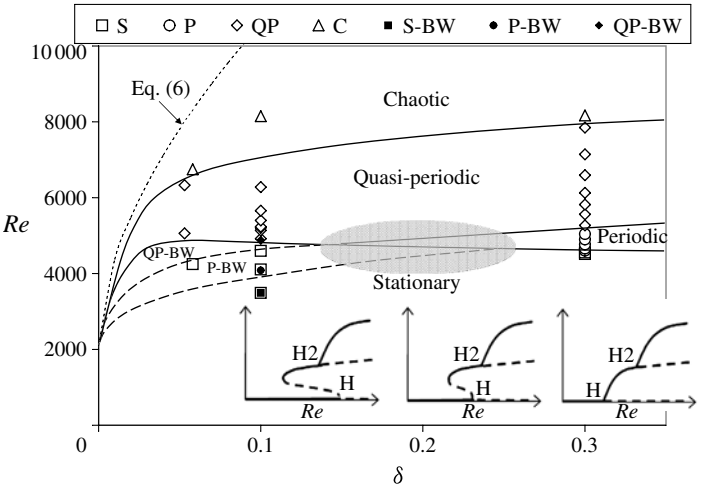

FIGURE 30. Tentative flow regime map in the Re–δ plane. Symbols: computational or experimental results classified as S (stationary), P (periodic), QP (quasi-periodic) or C (chaotic). S-BW, P-BW and QP-BW denote S, P or QP solutions obtained by letting Re decrease. Solid lines, transitions for increasing Re; dashed lines, transitions for decreasing Re. Bifurcation diagrams corresponding to different intervals of δ are drawn in the lower part of the figure. The grey region is hypothetical.

secondary Hopf bifurcation from periodic to quasi-periodic flow. The details of the flow regime map in the region of curvatures intermediate between 0.1 and 0.3 are purely hypothetical as suggested by the shaded area. Moreover, a complete regime map would exhibit a finely serrated shape of the transition curves in correspondence with the discrete jump in the number of wavelengths of either mode I or mode II as δ and Re vary, much as in the spiral Poiseuille flow study by Avila, Meseguer & Marques (2006): see e.g. figure 3 therein.

The transition criteria proposed in the literature and reviewed in § 2.1, mainly based on the behaviour of the friction coefficient, can now be revisited in light of the present results. Of course, a necessary assumption is that results actually obtained for helically coiled pipes of moderate torsion can be applied to toroidal pipes as well. The criterion expressed by (1.6) is reported in figure 30. For any curvature, it predicts a transitional Reynolds number far larger than that associated with transition to chaotic flow on the basis of the present work and of the existing literature. This suggests that (1.6) identifies not the onset of turbulence, but rather the attainment of turbulence levels sufficiently high for pressure drop to be dominated by turbulence effects. In fact, in configurations characterized by the presence of secondary flow, pressure drop is largely caused by recirculation and may be significantly higher than in parallel flow also under stationary laminar conditions; the appearance of unsteadiness, and even of turbulence, results in an added frictional term which increases gradually with the Reynolds number and, in low-turbulence flows, may represent just a minor contribution to the overall pressure drop.

This assumption is supported by figure 31, which reports the friction coefficient f as a function of Re for all the test cases studied at $\delta = 0.3$ and 0.1. For $\delta = 0.1$, Ito's laminar and turbulent correlations, (1.4) and (1.5), are also reported, while they are not applicable for $\delta = 0.3$. Equation (1.4) reproduces the present results for $\delta = 0.1$ with high accuracy. However, the most striking feature of figure 31 is that, for both

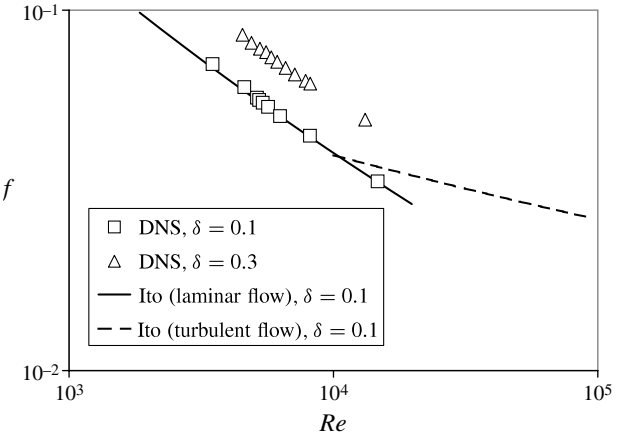

FIGURE 31. Darcy friction coefficient for two values of the curvature ($\delta = 0.1$ and 0.3). Solid lines, Ito correlation for laminar flow, equation (1.4); dashed lines, Ito correlation for turbulent flow, equation (1.5); symbols, present computational results.

curvatures and independent of the comparison with existing correlations, the present results do not exhibit any change in their trends in correspondence with the transition from stationary to unsteady laminar flow and to chaotic flow, thus confirming that the corresponding unsteady phenomena, up to low turbulence, are not sufficiently intense to affect the overall dissipation significantly. This also explains why criterion (1.6) predicts an increase in the transitional Re with the curvature δ, while the present results indicate transition values that vary non-monotonically with the curvature.

Finally, the issue of the adequacy of toroidal pipe flow as a model for more general curved pipe flows, mentioned in the Introduction, can now be re-examined in light of the present computational results and the literature. No previous study presents a comparable level of detail, so specific quantitative comparisons are not possible. However, all the present findings are compatible with published experimental and computational results. In particular, the features and the approximate wavelength of travelling modes for certain Reynolds numbers and curvatures are in agreement with the visualization studies by Webster & Humphrey (1997), conducted on helical coils (see § 1.2), and with the numerical simulations by the same authors, conducted for a finite tract of a curved pipe (see § 1.4). They are also compatible with the flow visualizations by Del Pino *et al.* (2008), conducted in a closed torus but under non-equilibrium conditions (decelerating flow), which show similar spatial travelling structures. Therefore, from a qualitative point of view neither a finite torsion nor a finite pipe length or even a departure from equilibrium conditions seems to modify too radically the basic phenomenology with respect to the present predictive study.

Of course, the choice of identifying the computational domain with a full torus, i.e. assuming 2π periodicity, imposes a precise wavelength selection on the travelling structures; in any finite-length simulation, differences in wave length and wave speed are to be expected. Ideally, only an infinite-length bend would not impose constraints on the streamwise travelling-wave structures; but this is not realizable in the absence of torsion. In their turn, pipes with torsion (helical coils) will exhibit a breakdown of the top–bottom symmetry, so that travelling-wave structures identical to those predicted here for zero torsion are not possible, and a more complex behaviour is to be expected.

REFERENCES

AVILA, M., MESEGUER, A. & MARQUES, F. 2006 Double Hopf bifurcation in corotating spiral Poiseuille flow. *Phys. Fluids* **18**, 064101.

BARUA, S. N. 1963 On the secondary flow in stationary curved pipes. *Q. J. Mech. Appl. Math.* **16**, 61–77.

BERGER, S. A., TALBOT, L. & YAO, L. S. 1983 Flow in curved pipes. *Ann. Rev. Fluid Mech.* **15**, 461–512.

BERKOOZ, G., HOLMES, P. & LUMLEY, J. L. 1993 The proper orthogonal decomposition in the analysis of turbulent flows. *Annu. Rev. Fluid Mech.* **25**, 539–575.

BOUSSINESQ, M. J. 1868 Mémoire sur l'influence des frottements dans les mouvements régulier des fluids. *J. Math. Pures Appl. 2me Sér.* **13**, 377–424.

CHANDRASEKAR, S. 1970 *Hydrodynamic and Hydromagnetic Stability*, 3rd printing. Oxford University Press.

CHEN, W. H. & JAN, R. 1992 The characteristics of laminar flow in a helical circular pipe. *J. Fluid Mech.* **244**, 241–256.

CHOI, H. & MOIN, P. 1994 Effects of the computational time step on numerical solutions of turbulent flow. *J. Comput. Phys.* **113**, 1–4.

CIONCOLINI, A. & SANTINI, L. 2006 An experimental investigation regarding the laminar to turbulent flow transition in helically coiled pipes. *Exp. Therm. Fluid Sci.* **30**, 367–380.

COLLINS, W. M. & DENNIS, S. C. R. 1975 The steady motion of a viscous fluid in a curved tube. *Q. J. Mech. Appl. Math.* **28**, 133–156.

DASKOPOULOS, P. & LENHOFF, A. M. 1989 Flow in curved ducts: bifurcation structure for stationary ducts. *J. Fluid Mech.* **203**, 125–148.

DEAN, W. R. 1927 Note on the motion of the fluid in a curved pipe. *Phil. Mag.* **4**, 208–223.

DEL PINO, C., HEWITT, R. E., CLARKE, R. J., MULLIN, T. & DENIER, J. P. 2008 Unsteady fronts in the spin-down of a fluid-filled torus. *Phys. Fluids* **20**, 124104.

DENNIS, S. C. R. & NG, M. 1982 Dual solution for steady laminar flow through a curved tube. *Q. J. Mech. Appl. Math.* **35**, 305–324.

EINSTEIN, A. 1926 Die Ursache der Mäanderbildung der Flußläufe und des sogenannten Baerschen Gesetzes. *Naturwissenschaften* **11**, 223–224.

EUSTICE, J. 1911 Experiment of streamline motion in curved pipes. *Proc. R. Soc. Lond.* A **85**, 119–131.

FENSTERMACHER, P. R., SWINNEY, H. L. & GOLLUB, J. P. 1979 Dynamic instability and the transition to chaotic Taylor vortex flow. *J. Fluid Mech.* **94**, 103–128.

FRIEDRICH, R., HÜTTL, T. J., MANHART, M. & WAGNER, C. 2001 Direct numerical simulation of incompressible turbulent flows. *Comput. Fluids* **30**, 555–579.

FUSEGI, T., HYUN, J. M. & KUWAHARA, K. 1992 Three-dimensional numerical simulation of periodic natural convection in a differentially heated cubical enclosure. *Appl. Sci. Res.* **49**, 271–282.

GERMANO, M. 1982 On the effect of torsion in a helical pipe flow. *J. Fluid Mech.* **125**, 1–8.

GOLLUB, J. P. & BENSON, S. V. 1980 Many routes to turbulent convection. *J. Fluid Mech.* **100**, 449–470.

GRINDLEY, J. H. & GIBSON, A. H. 1908 On the frictional resistance to the flow of air through a pipe. *Proc. R. Soc. Lond.* A **80**, 114–139.

HUNT, J. C. R., WRAY, A. A. & MOIN, P. 1988 Eddies, streams, and convergence zones in turbulent flows. In *Proc. 1988 Summer Program*, Report CTR-S88. NASA Center for Turbulence Research.

HÜTTL, T. J. & FRIEDRICH, R. 2001 Direct numerical simulation of turbulent flows in curved and helically coiled pipes. *Comput. Fluids* **30**, 591–605.

HÜTTL, T. J., CHAUDURI, M., WAGNER, C. & FRIEDRICH, R. 2004 Reynolds-stress balance equations in orthogonal helical coordinates and application. *Z. Angew. Math. Mech.* **84**, 403–416.

ITO, H. 1959 Friction factors for turbulent flow in curved pipes. *Trans. ASME: J. Basic Engng.* **81**, 123–134.

JAYANTI, S. & HEWITT, G. F. 1991 On the par adox concerning friction factor ratio in laminar flow in coils. *Proc. R. Soc. Lond. Ser.* A **432**, 291–299.

JINSUO, Z. & BENZHAO, Z. 1999 Fluid flow in a helical pipe. *Acta Mechanica Sin.* **15**, 299–312.

KAO, H. C. 1987 Torsion effect on fully developed flow in a helical pipe. *J. Fluid Mech.* **184**, 335–356.

KERSWELL, R. R. 2005 Recent progress in understanding the transition to turbulence in a pipe. *Nonlinearity* **18**, R17–R44.

KNIGHTLY, G. H. & SATHER, D. 1993 Periodic waves in rotating plane Couette flow. *Z. Angew. Math. Phys.* **44**, 1–16.

LARRAIN, J. & BONILLA, C. F. 1970 Theoretical analysis of pressure drop in the laminar flow of fluid in a coiled pipe. *Trans. Soc. Rheol.* **14**, 135–147.

LUMLEY, J. L. 1967 The structure of inhomogeneous turbulence. In *Atmospheric Turbulence and Wave Propagation* (ed. A. M. Monin & V. I. Tatarski), pp. 166–178. Nauka.

MCCONALOGUE, D. J. & SRIVASTAVA, R. S. 1968 Motion of fluid in a curved tube. *Proc. R. Soc. Lond.* A **307**, 37–53.

MEES, P. A. J., NANDAKUMAR, K. & MASLIYAH, J. H. 1996 Secondary instability of flow in a curved duct of square cross-section. *J. Fluid Mech.* **323**, 387–409.

MORI, Y. & NAKAYAMA, W. 1965 Study on forced convective heat transfer in curved pipes. *Intl J. Heat Mass Transfer* **8**, 67–82.

NAPHON, P. & WONGWISES, S. 2006 A review of flow and heat transfer characteristics in curved tubes. *Renewable and Sustainable Energy Rev.* **10**, 463–490.

NARASIMHA, R. & SREENIVASAN, K. R. 1979 Relaminarization of fluid flows. *Adv. Appl. Mech.* **19**, 221–309.

RAYLEIGH, LORD 1920 On the dynamics of revolving fluids. *Scientific Papers* **6**, 447–453.

SIGGERS, J. H. & WATERS, S. L. 2008 Unsteady flows in pipes with finite curvatures. *J. Fluid Mech.* **600**, 133–165.

SREENIVASAN, K. R. & STRYKOWSKI, P. J. 1983 Stabilization effects in flow through helically coiled pipes. *Exp. Fluids* **1**, 31–36.

SRINIVASAN, S., NADAPURKAR, S. & HOLLAND, F. A. 1970 Friction factors for coils. *Trans. Inst. Chem. Engrs* **48**, T 156–T 161.

TAYLOR, G. I. 1929 The criterion for turbulence in curved pipes. *Proc. R. Soc.* **124** (794), 243–249.

THOMSON, J. 1876 On the origin of windings of rivers in alluvial plains, with remarks on the flow of water round bends in pipes. *Proc. R. Soc. Lond.* A **25**, 5–8.

VAN DYKE, M. 1978 Extended Stokes series: laminar flow through a loosely curved pipe. *J. Fluid Mech.* **86**, 129–145.

VASHISTH, S., KUMAR, V. & NIGAM, D. P. K. 2008 A review on the potential application of curved geometries in process industry. *Ind. Engng Chem. Res.* **47**, 3291–3337.

WANG, L. & YANG, T. 2004 Bifurcation and stability of forced convection in curved ducts of square cross-section. *Intl J. Heat Mass Transfer* **47**, 2971–2987.

WEBSTER, D. R. & HUMPHREY, J. A. C. 1993 Experimental observations of flow instability in a helical coil. *Trans. ASME: J. Fluids Engng* **115**, 436–443.

WEBSTER, D. R. & HUMPHREY, J. A. C. 1997 Travelling wave instability in helical coil flow. *Phys. Fluids* **9**, 407–418.

WHITE, C. M. 1929 Flow through curved pipes. *Proc. R. Soc.* **123** (792), 645–663.

WILLIAMS, G. S., HUBBELL, C. W. & FENKELL, G. H. 1902 On the effect of curvature upon the flow of water in pipes. *Trans. ASCE* **47**, 1–196.

XIE, G. D. 1990 Torsion effect on secondary flow in helical pipes. *Intl J. Heat Fluid Flow* **11**, 114–119.

YAMAMOTO, K., AKITA, T., IKEUKI, H. & KITA, Y. 1995 Experimental study of the flow in a helical circular tube. *Fluid Dynam. Res.* **16**, 237–249.

YANASE, S., GOTO, N. & YAMAMOTO, K. 1989 Dual solution of the flow through a curved pipe. *Fluid Dynam. Res.* **5**, 191–201.

YANASE, S., YAMAMOTO, K. & YOSHIDA, T. 1994 Effect of curvature on dual solutions of flow through a curved circular tube. *Fluid Dynam. Res.* **13**, 217–228.

ZABIELSKI, L. & MESTEL, A. J. 1998 Steady flow in a helically symmetric pipe. *J. Fluid Mech.* **370**, 297–320.